Remote Sensing of Environment 176 (2016) 255–271

Contents lists available at ScienceDirect

Remote Sensing of Environment

journal homepage: www.elsevier.com/locate/rse

A general method to normalize Landsat reflectance data to nadir BRDF adjusted reflectance

D.P. Roy [a,*], H.K. Zhang [a], J. Ju [b,c], J.L. Gomez-Dans [d,e], P.E. Lewis [d,e], C.B. Schaaf [f], Q. Sun [f], J. Li [a], H. Huang [a], V. Kovalskyy [a]

[a] Geospatial Science Center of Excellence, South Dakota State University, Brookings, SD 57007, USA
[b] Universities Space Research Association, 7178 Columbia Gateway Dr, Columbia, MD 21046, USA
[c] NASA Goddard Space Flight Center, 8800 Greenbelt Rd, Greenbelt, MD 20771, USA
[d] NERC National Centre for Earth Observation (NCEO), UK
[e] Department of Geography, University College London, Gower Street, London WC1E 6BT, UK
[f] School for the Environment, University of Massachusetts Boston, Boston, MA 02125, USA

ARTICLE INFO

Article history:
Received 31 October 2015
Received in revised form 23 January 2016
Accepted 28 January 2016
Available online 13 February 2016

Keywords:
Bidirectional reflectance distribution function (BRDF)
Landsat
NBAR
MODIS

ABSTRACT

The Landsat satellites have been providing spectacular imagery of the Earth's surface for over 40 years. However, they acquire images at view angles ±7.5° from nadir that cause small directional effects in the surface reflectance. There are also variations with solar zenith angle over the year that can cause apparent change in reflectance even if the surface properties remain constant. When Landsat data from adjoining paths, or from long time series are used, a model of the surface anisotropy is required to adjust all Landsat observations to a uniform nadir view (primarily for visual consistency, vegetation monitoring, or detection of subtle surface changes). Here a generalized approach is developed to provide consistent view angle corrections across the Landsat archive. While this approach is not applicable for generation of Landsat surface albedo, which requires a full characterization of the surface bidirectional reflectance distribution function (BRDF), or for correction to a constant solar illumination angle across a wide range of sun angles, it provides Landsat nadir BRDF-adjusted reflectance (NBAR) for a range of terrestrial monitoring applications.

The Landsat NBAR is derived as the product of the observed Landsat reflectance and the ratio of the reflectances modeled using MODIS BRDF spectral model parameters for the observed Landsat and for a nadir view and fixed solar zenith geometry. In this study, a total of 567 conterminous United States (CONUS) January and July 2010 Landsat 5 Thematic Mapper (TM) and Landsat 7 Enhanced Thematic Mapper (ETM+) images that have swath edge overlapping paths sensed in alternating backscatter and forward scattering orientations were used. The average difference between Landsat 5 TM and Landsat 7 ETM+ surface reflectance in the forward and backward scatter directions at the overlapping Landsat scan edges was quantified. The CONUS July view zenith BRDF effects were about 0.02 in the Landsat visible bands, and about 0.03, 0.05 and 0.06, in the 2.1 μm, 1.6 μm and near-infrared bands respectively. Comparisons of Landsat 5 TM and Landsat 7 ETM+ NBAR derived using MODIS BRDF spectral model parameters defined with respect to different spatial and temporal scales, and defined with respect to different land cover types, were undertaken. The results suggest that, because the BRDF shapes of different terrestrial surfaces are sufficiently similar over the narrow 15° Landsat field of view, a fixed set of MODIS BRDF spectral model parameters may be adequate for Landsat NBAR derivation with little sensitivity to the land cover type, condition, or surface disturbance. A fixed set of BRDF spectral model parameters, derived from a global year of highest quality snow-free MODIS BRDF product values, are provided so users may implement the described Landsat NBAR generation method.

1. Introduction

Landsat data offer a unique 40+ year record of the terrestrial surface (Roy et al., 2014). Recently, there has been a significant increase in the development of techniques using dense Landsat time series to describe surface land cover type, condition and dynamics (Boschetti, Roy, Justice, & Humber, 2015; Brooks, Thomas, Wynne, & Coulston, 2012; Hansen & Loveland, 2012; Hansen et al., 2014; Yan & Roy, 2014; Zhu, Woodcock, & Olofsson, 2012) and the development of spatially mosaiced and temporally composited Landsat reflectance products that use a significant proportion of the available Landsat data (Griffiths, van der Linden, Kuemmerle, & Hostert, 2013; Lindquist, Hansen, Roy, &

* Corresponding author.

http://dx.doi.org/10.1016/j.rse.2016.01.023

Justice, 2008; Roy et al., 2010). This has been made possible by the free availability of systematically geolocated (Lee, Storey, Choate, & Hayes, 2004; Storey, Choate, & Lee, 2014) and radiometrically calibrated (Markham & Helder, 2012) Landsat data and also in some cases by algorithms for Landsat atmospheric correction (Masek et al., 2006; Ouaidrari & Vermote, 1999) and cloud detection (Irish, Barker, Goward, & Arvidson, 2006; Scaramuzza, Bouchard, & Dwyer, 2012; Zhu & Woodcock, 2012). Algorithms for the correction of the directional dependency of Landsat reflectance have received less attention however. Arguably this is because directional reflectance effects, commonly described by the bidirectional reflectance distribution function (BRDF) (units of sr^{-1}), are relatively small in Landsat data, due to the narrow 15° sensor field of view and also because the acquisition view zenith angle is usually less than the solar zenith angle and so Landsat reflectance hot-spot effects do not occur (Zhang et al. in press).

Most terrestrial surfaces are not Lambertian and so directional reflectance effects are present in satellite reflectance retrievals due to variable solar-surface-sensor geometry. Terrestrial reflectance anisotropy varies with the physical arrangement, structural variability, and optical properties of the surface components (soil, grass, trees, etc.) and nominally may vary with the land cover type and condition (Gao, Schaaf, Strahler, Jin, & Li, 2003; Roberts, 2001). The BRDF of terrestrial surfaces can be broadly described by dome-bowl anisotropic reflectance shapes (basis functions) with a retro-reflectance peak (hot spot) that describes the increased directional reflectance associated with shadow hiding that occurs when the solar and view direction coincide (Hautecœur & Leroy, 1998; Jackson et al., 1990; Li & Strahler, 1992; Maignan, Bréon, & Lacaze, 2004; Rahman, Verstraete, & Pinty, 1993; Roujean, Leroy, & Deschamps, 1992). Models of the BRDF of terrestrial surfaces are commonly inverted against multiple cloud-cleared, atmospherically-corrected directional reflectance values that sufficiently sample this anisotropy. Inversion over snow covered surfaces may be less reliable because snow can exhibit significant forward scattering particularly in the near and short wave infrared (Aoki et al., 2000; Warren, Brandt, & Hinton, 1998). Bacour and Bréon (2005) observed that only a limited number of archetypal BRDF shapes (typically five in the red and near infrared) capture most of the variability of the directional reflectance observed in snow-free coarse resolution POLarization and Directionality of the Earth's Reflectances (POLDER) data (view zenith angles up to 70°). Similarly, Jiao et al. (2014) and Zhang et al. (2015) observed that six archetypal BRDF shapes can be generally identified in snow-free Moderate Resolution Imaging Spectroradiometer (MODIS) data (view zenith angles up to 65°).

Empirical statistical correction methods to minimize Landsat BRDF effects have been developed and they require the presence of similar land cover types or pseudo-invariant features located across each image (Broich et al., 2011; Hansen et al., 2008; Toivonen, Kalliola, Ruokolainen, & Malik, 2006). However, such features are not always available and images normalized in this manner are only comparable reliably to other images within the normalized data set. More globally applicable approaches that employ external BRDF information derived from the MODIS BRDF/Albedo product suite (Schaaf, Liu, Gao, & Strahler, 2011; Schaaf et al., 2002) have been advocated (Flood, Danaher, Gill, & Gillingham, 2013; Gao et al., 2014; Li et al., 2010; Roy et al., 2008). They normalize observed Landsat reflectance to nadir (0° view zenith) and a specified solar zenith angle to generate Landsat nadir BRDF adjusted reflectance (NBAR). A *c-factor* approach, similar to that proposed by Flowerdew and Haigh (1995) and first described for Landsat application by Roy et al. (2008), is used, whereby Landsat NBAR is derived as the product of the observed Landsat reflectance and the ratio of the reflectances modeled using contemporaneous MODIS BRDF spectral model parameters for the observed Landsat and for a nadir view and fixed solar zenith geometry. The *c-factor* approach is applied on a per-pixel basis and is unaffected by the presence of missing or contaminated neighboring Landsat pixels, does not require the presence of pseudo-invariant features or similar land cover types across each image, accommodates spatial and temporal surface dynamics that are observable at the 500 m MODIS BRDF/Albedo gridded product resolution, and may be automated without the need for tuning parameters (Roy et al., 2008). Note that the *c-factor* BRDF normalization is not applicable to sensors with large view angle variations, such as the MODIS and Visible Infrared Imaging Radiometer Suite (VIIRS) scanning instruments, nor for the normalization of significant solar illumination variations.

Recently, researchers have suggested, based on examination of limited amounts of satellite data, that spatially and temporally explicit MODIS BRDF spectral model parameters used to *c-factor* normalize Landsat imagery perform no better than using a fixed set of BRDF spectral model parameters (Flood, 2013; Flood et al., 2013). Claverie et al. (2015) demonstrated similar findings over sample land covers using a sample of 28.0° maximum viewing zenith angle Satellite Pour l'Observation de la Terre (SPOT-4) images. Potentially, the BRDF shapes of terrestrial surfaces may be sufficiently similar over the 15° Landsat field of view that a *c-factor* BRDF normalization approach may be applied reliably using only a single fixed set of MODIS BRDF spectral model parameters. If this is the case then Landsat NBAR can be derived in a computationally efficient manner for all the Landsat global long-term record and not just from February 2000 onwards when the MODIS products became first available (Justice et al., 2002).

In this paper the MODIS BRDF/Albedo model parameter and MODIS land cover products, and Landsat 5 Thematic Mapper (TM) and Landsat 7 Enhanced Thematic Mapper Plus (ETM+) data, are used to derive and examine the utility of a single fixed set of BRDF spectral model parameters for Landsat NBAR generation. The satellite data and pre-processing are described, and then the evaluation methods and results, including a quantification of the magnitude of Landsat view zenith BRDF effects observed across the conterminous United States (CONUS), are presented. The Landsat BRDF normalization sensitivity to the use of MODIS BRDF spectral model parameters defined with respect to different spatial (CONUS and global) and temporal (weekly and annual) scales, and defined with respect to different land cover types, is reported. A general method to normalize Landsat reflectance data to NBAR is suggested and the recommended MODIS BRDF derived spectral model parameters are provided for users to implement. The paper concludes with a discussion and the implications of the research.

2. Data

2.1. Landsat TM and ETM + data

The Landsat 5 and 7 satellites are in the same approximately 710 km sun-synchronous circular 98.2° inclined orbit and overpass every Earth location every 16 days but are offset from each other by 8 days (Loveland & Dwyer, 2012; Teillet et al., 2001). The Landsat 5 TM and Landsat 7 ETM+ sensors have 15° field of view and their data are available in approximately 185 km × 180 km scenes defined in a Worldwide Reference System (WRS) of path (groundtrack parallel) and row (latitude parallel) coordinates (Arvidson, Goward, Gasch, & Williams, 2006). In May 2003 the Landsat 7 ETM+ scan line corrector failed, reducing the usable data in each Landsat ETM+ image by 22% (Markham, Storey, Williams, & Irons, 2004). The Landsat 5 TM has no such missing data issue. The Landsat 5 sensor acquired data from 1984 until 2012 while the Landsat 7 instrument is still operational. The Landsat 5 and 7 acquisitions are nominally processed to Level 1 terrain corrected (L1T) level with processing that includes radiometric correction, systematic geometric correction, precision correction using ground control, and the use of a digital elevation model to correct parallax error due to local topographic relief (Lee et al., 2004). The Landsat 5 TM and 7 ETM+ radiometric calibration uncertainties are reported as 7% and 5% respectively (Markham & Helder, 2012) and over the CONUS their geolocation error is less than one 30 m pixel (Lee et al., 2004).

All the Landsat 5 and Landsat 7 acquisitions for a CONUS winter week (8th to 14th January 2010) and summer week (2nd to 8th July

2010) were obtained from the U.S. Landsat archive. Summer and winter images were used to capture phenological surface differences and therefore a range of surface anisotropy. Only Landsat acquisitions processed to L1T and with metadata GEOMETRIC_RMSE_MODEL values ≤30 m were used to ensure the high geolocation accuracy needed for a pixel-level Landsat 5 and 7 data comparison. In addition, only daytime acquisitions, defined as those with metadata SUN_ELEVATION values >5°, were used. This resulted in 270 Landsat 5 TM images (124 winter, 146 summer) and 297 Landsat 7 ETM+ images (139 winter, 158 summer), a total of 567 images.

Fig. 1 illustrates the geographic locations of the Landsat data. There is an across-track acquisition overlap that increases further north due to the poleward convergence of the Landsat orbits (Kovalskyy & Roy, 2013). Because the TM and ETM+ are in the same orbit but offset by 8 days the western and eastern sides of a sensor acquisition are overlapped by the eastern and western sides respectively of the other sensor acquisition, and are acquired with only a one-day separation. This is important for the analysis in this paper as the overlapping area is sensed in the forward scattering direction from one sensor and the backward scattering direction from the other, and this pattern alternates across the CONUS. The one-day separation is advantageous as surface changes are less likely to occur within such a short period, although atmospheric conditions may change.

2.2. MODIS BRDF/Albedo product

The 16-day 500 m MODIS BRDF model parameter product (MCD43A1) was used to compute the directional reflectance at any

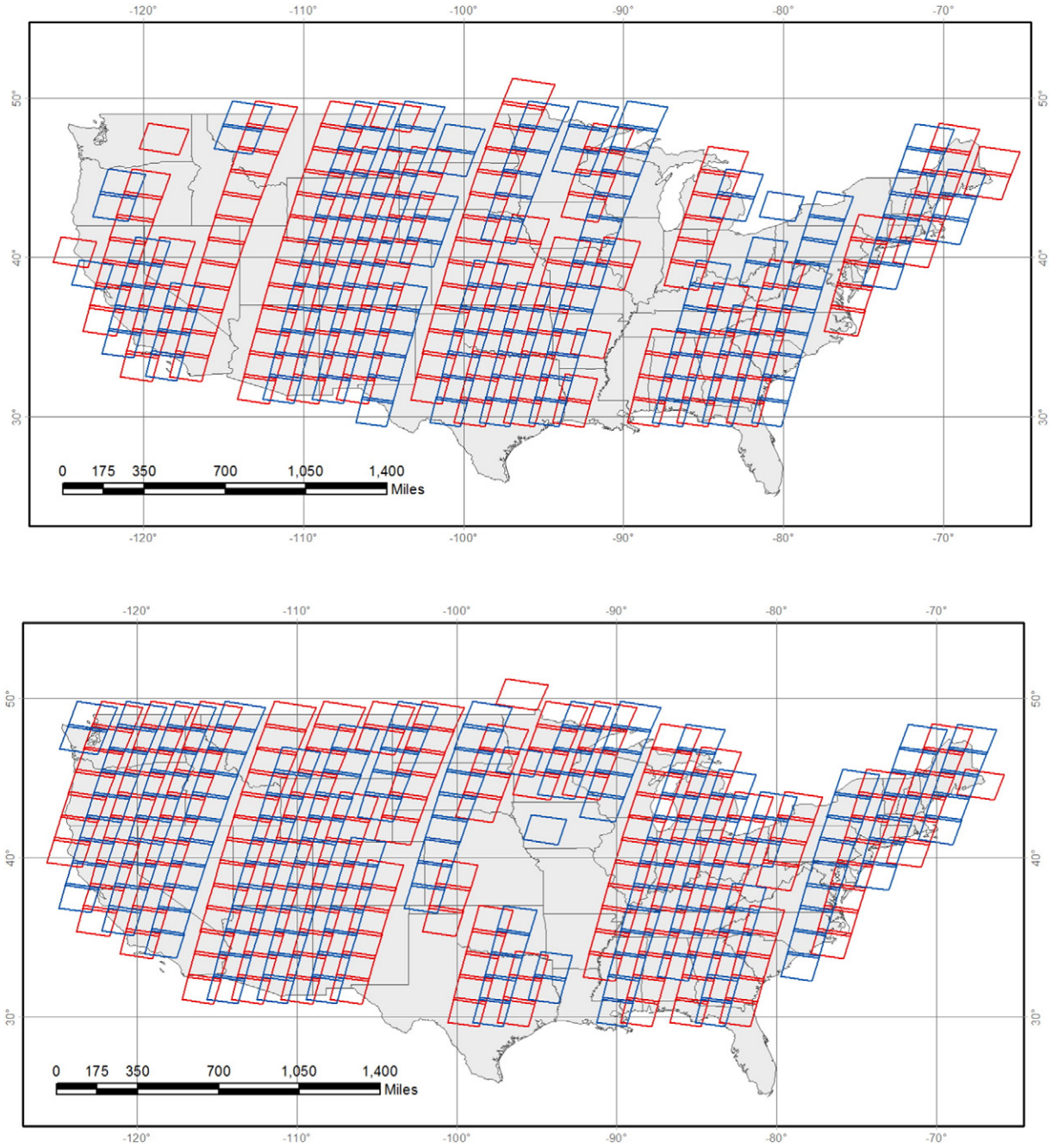

Fig. 1. Geographic locations of the Landsat 5 TM (blue) and Landsat 7 ETM+ (red) images for the winter January 8th to 14th, 2010 (top) and summer July 2nd to 8th, 2010 (bottom) weeks. Locations were derived from the latitude and longitude scene corner coordinate image metadata.

desired viewing and solar geometry. The product defines Ross-Thick/Li-Sparse-Reciprocal spectral model parameters determined as those that best fit all of the cloud-cleared, atmospherically-corrected MODIS Terra and Aqua reflectance values observed at each pixel location over a 16 day period (Schaaf et al., 2002, 2011). The Ross-Thick/Li-Sparse-Reciprocal BRDF model defines reflectance as a weighted sum of an isotropic parameter and two functions (or kernels) of viewing and illumination geometry (Roujean et al., 1992), where one kernel is derived from radiative transfer models (Ross, 1981) and the other is based on surface scattering and geometric shadow casting theory (Li & Strahler, 1992) as:

$$\rho(\lambda_{MODIS}, \Omega, \Omega') = f_{iso}(\lambda_{MODIS}) + f_{vol}(\lambda_{MODIS})K_{vol}(\Omega, \Omega') + f_{geo}(\lambda_{MODIS})K_{geo}(\Omega, \Omega') \quad (1)$$

where $\rho(\lambda_{MODIS}, \Omega, \Omega')$ is the MODIS spectral reflectance for wavelength λ_{MODIS}, for viewing vector Ω (view zenith and azimuth angles) and solar illumination vector Ω' (solar zenith and azimuth angles), $K_{vol}(\Omega, \Omega')$ and $K_{geo}(\Omega, \Omega')$ are the volumetric scattering and geometric-optical model kernels respectively which depend only on the sun-view geometry (Ω, Ω'), and $f_{iso}(\lambda_{MODIS})$, $f_{vol}(\lambda_{MODIS})$, $f_{geo}(\lambda_{MODIS})$ are spectrally dependent BRDF model parameters (Schaaf et al., 2002, 2011). Generally, the volumetric scattering kernels represent bowl BRDF shapes while the geometric-optical kernels represent more domed BRDF shapes. The volumetric scattering and geometric-optical model kernels are quite uniform and comparatively similar over the near-nadir portions of the bi-directional reflectance distribution (Lucht, Schaaf, & Strahler, 2000). This is illustrated in Fig. 2 which shows for different solar zenith angles (colored lines) the very high degree of correlation between these kernels derived over the Landsat ±7.5° view zenith range (values along lines). This linear relationship implies that over such a narrow view angle range, the two kernels effectively collapse to a single kernel.

The gridded 500 m Collection 5 MCD43A1 and MCD43A2 products were used in this study. They were generated with a quasi-rolling production strategy, whereby each 16-day product is produced every 8 days on an 8-day overlapping basis to minimize global data processing constraints (Roy, Lewis, Schaaf, Devadiga, & Boschetti, 2006). The three MCD43A1 BRDF spectral model parameters, i.e. $f_{i=1\ldots3}(\lambda_{MODIS})$, for the MODIS 500 m land surface reflectance bands: blue (0.459–0.479 μm), green (0.545–0.565 μm), red (0.620–0.670 μm), near-infrared (0.841–0.876 μm) and shortwave infrared (1.628–1.654 μm and 2.105–2.155 μm) were used; the spectral parameters for the MODIS 1.230-1.250 μm band were not used since this band has no corresponding Landsat 5 or 7 band (Roy et al., 2008). The MODIS BRDF/Albedo quality product (MCD43A2) corresponding to each MCD43A1 product was used to remove poor quality product values. These MODIS products are defined in 10° × 10° tiles in the equal area sinusoidal projection (Wolfe, Roy, & Vermote, 1998). All of the MODIS MCD43A1 and MCD43A2 products for 2010 over the CONUS and globally were used. This corresponded to a total of 11 MODIS tiles (CONUS) and an average of 310 tiles (globally) every 8 days for all of 2010.

2.3. MODIS land cover product

The Collection 5 annual 500 m MODIS land cover product (MCD12Q1) (Friedl et al., 2010) was used for land cover type specific BRDF normalization analyses. The MCD12Q1 International Geosphere–Biosphere Program (IGBP) scheme, which classifies each 500 m pixel into one of the 17 classes (Table 1) and has a reported 75% overall land cover classification accuracy, was used. The classes are mutually exclusive and every land pixel is either classified into one class or is unclassified. Associated with this classification scheme is a per-pixel classification confidence estimate (range 0–100) (McIver & Friedl, 2001) that was used in this study to remove pixels with low classification confidence. Eleven years (2002 to 2012) of MCD12Q1 over the CONUS was used to identify regions of relatively little surface land cover change. This corresponded to a total of 11 MODIS tiles per year defined in the equal area sinusoidal projection.

3. Data pre-preprocessing

3.1. Overview

A number of pre-processing steps were undertaken to enable meaningful BRDF normalization of the Landsat 5 TM and 7 ETM+ data using the MODIS BRDF spectral model parameters. The Landsat data were converted to top of atmosphere (TOA) reflectance and then atmospherically corrected to surface reflectance. The Landsat data were projected into the MODIS sinusoidal projection. Only spatially overlapping pairs of Landsat 5 TM and Landsat 7 ETM+ reflectance values sensed one day apart were considered; the pairs have similar solar geometry but different viewing geometries. Only pairs that were cloud-free, snow-free, unsaturated, and that had no significant change in their one day separation, were considered. Only one 30 m Landsat 5 and 7 reflectance pair

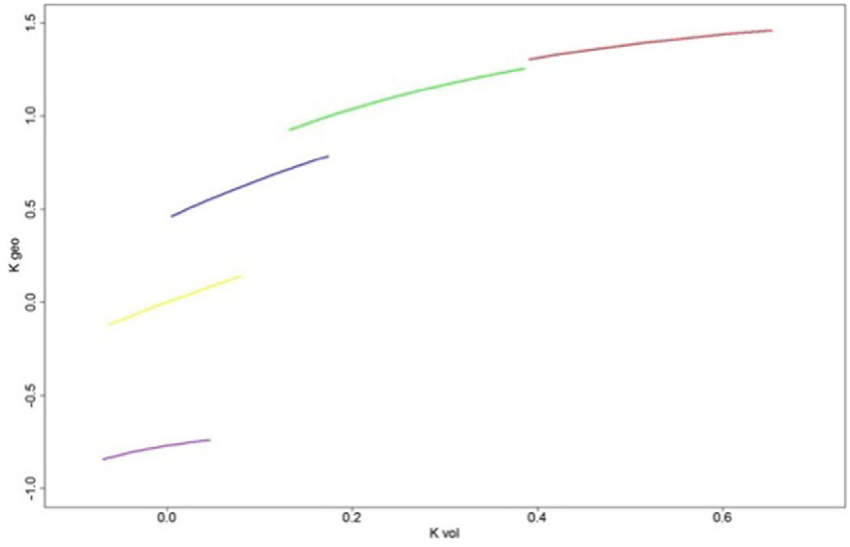

Fig. 2. Plots of the MODIS Ross-Thick/Li-Sparse-Reciprocal BRDF geometric kernel (K_{geo}) as a function of the volumetric kernel (K_{vol}) for Landsat view zenith angles from −7.5° to 7.5° (colored lines) in the principal plane (0° relative azimuth) for solar zenith angles 0° (red), 15° (green), 30° (blue), 45° (yellow), and 60° (purple). The Pearson correlation between the K_{geo} and K_{vol} data in each colored line is greater than 0.99.

Table 1
The 17 MODIS MCD12Q1 IGBP land cover classes (Friedl et al., 2010).

Class	Name	Class	Name
0	Water	9	Savannas
1	Evergreen needleleaf forest	10	Grasslands
2	Evergreen broadleaf forest	11	Permanent wetlands
3	Deciduous needleleaf forest	12	Croplands
4	Deciduous broadleaf forest	13	Urban and built-up
5	Mixed forest	14	Cropland/natural vegetation mosaic
6	Closed shrublands	15	Snow and ice
7	Open shrublands	16	Barren or sparsely vegetated
8	Woody savannas		

per MODIS 500 m pixel was used to reduce the data volume and to provide a convenient way to investigate the use of MODIS BRDF spectral model parameters for different land cover types. The normalization was undertaken using only the highest quality snow-free MODIS spectral BRDF model parameters.

3.2. Landsat reflectance data pre-processing

The CONUS Landsat L1T data were converted to top of atmosphere reflectance and then atmospherically corrected to surface reflectance using the Landsat Ecosystem Disturbance Adaptive Processing System (LEDAPS) code (Masek et al., 2006). It is well established that atmospheric correction is required prior to BRDF correction because atmospheric gases and aerosols scatter and absorb radiation anisotropically (Franch, Vermote, Sobrino, & Fédèle, 2013; Hu, Lucht, & Strahler, 1999). Moreover, atmospheric gases and aerosols are highly variable in space and time and may have significant impacts on Landsat top of atmosphere reflectance (Masek et al., 2006; Roy et al., 2016) that can be greater than the BRDF effects found in this paper.

Saturated reflectance values (associated mainly with pure snow acquisitions and residual cloud effects) were flagged based on the Landsat L1T digital numbers in each band, with saturation generally varying spectrally and with the illumination geometry (Bindschadler et al., 2008; Roy et al., 2010). Two per-pixel cloud masks were used, the heritage Landsat project automatic cloud cover assessment algorithm (ACCA) (Irish et al., 2006) and a decision tree cloud mask algorithm that generally performs better than ACCA for Landsat 7 ETM+ over the CONUS (Roy et al., 2010). Snow pixels were flagged in a way that is consistent with the MODIS snow detection algorithm (Hall, Riggs, Salomonson, DiGirolamo, & Bayr, 2002), specifically, snow was flagged if the normalized difference snow index (NDSI) > 0.4, near-infrared reflectance >0.11, and green reflectance >0.10, where the NDSI is the green minus shortwave infrared (1.65 μm) reflectance divided by their sum.

The Landsat per-pixel solar geometry was computed using an astronomical model (Blanco-Muriel, Alarcón-Padilla, López-Moratalla, & Lara-Coira, 2001) parameterized with each Landsat pixel latitude and longitude, date, and the Landsat acquisition time. The astronomical model is sufficiently accurate for the purposes of this study with a reported average and standard deviation solar zenith prediction error of 0.001 and 0.114 min of arc (Blanco-Muriel et al., 2001). The Landsat per-pixel viewing geometry was calculated using the Landsat Image Assessment System geometric libraries developed to monitor, characterize, and calibrate sensor and platform specific aspects of the Landsat satellite ETM+ sensor (Lee et al., 2004). The viewing vector was computed for each output pixel by first computing a vector normal to the surface of the WGS84 Earth model for the geodetic pixel coordinate, then the unit vector from the geodetic coordinate to the modeled satellite position, adjusting for the sensor-satellite attitude, and then the viewing vector zenith and azimuth components derived using standard trigonometric formulae (Roy et al., 2008).

3.3. Landsat projection to MODIS sinusoidal equal area projection and quality filtering

The pre-processed Landsat data (Section 3.2) were projected with nearest neighbor resampling into fixed 5295 × 5295 30 m pixel tiles in the MODIS sinusoidal equal area projection using the Web Enabled Landsat Data (WELD) processing software (Roy et al., 2010). In this way the projected Landsat data were aligned with the MODIS BRDF and land cover products. Each winter and summer week of Landsat 5 TM and 7 ETM+ data were projected independently because at CONUS latitudes each Landsat sensor observes a 30 m pixel location no more than once per week, but the edges of the Landsat 5 TM and 7 acquisitions ETM+ overlap with only a one-day separation (Fig. 1).

For the January and July Landsat data every pair of Landsat 5 and 7 reflectance values defined in the overlap (Fig. 1) at the same sinusoidal 30 m pixel location was examined. Only pairs that had values that were not flagged as cloudy, snow contaminated, or saturated (Section 3.2) were used. To remove any 30 m land cover and surface condition changes that may have occurred in the one day difference between the two Landsat sensors (due to abrupt disturbances such as fire, flooding, agricultural harvesting, and residual ephemeral snowfall) a filter was applied to their TOA blue reflectance and TOA Normalized Difference Vegetation Index (NDVI) values as:

$$\frac{\left|\mathrm{NDVI}^{\mathrm{ETM+}}-\mathrm{NDVI}^{\mathrm{TM}}\right|}{\left|\mathrm{NDVI}^{\mathrm{ETM+}}+\mathrm{NDVI}^{\mathrm{TM}}\right|/2}>0.15 \quad \mathrm{OR} \quad \frac{\left|\rho_{\mathrm{blue}}^{\mathrm{ETM+}}-\rho_{\mathrm{blue}}^{\mathrm{TM}}\right|}{\left|\rho_{\mathrm{blue}}^{\mathrm{ETM+}}+\rho_{\mathrm{blue}}^{\mathrm{TM}}\right|/2}>0.51. \tag{2}$$

The filter (Eq. (2)) rejects pixel values where the relative change in one day between sensors is greater than the average effect of the atmosphere on the Landsat NDVI or blue reflectance. The blue band is the shortest wavelength Landsat band and is the most sensitive to atmospheric effects. In a recent study considering approximately 53 million 30 m pixel locations sampled systematically across the CONUS for 12 months, the mean absolute difference between Landsat ETM+ surface and TOA reflectance expressed as percentages of the surface reflectance, and considering good quality atmospheric corrections only, was 15% for the NDVI and 51% for the blue band (Roy et al., 2014). This filtering is quite aggressive, but given the large amount of Landsat data considered and the study goals, this is preferable to retaining Landsat TM and ETM+ pairs that contained any change. The corresponding remaining pairs of Landsat surface reflectance values were then identified and used in the subsequent analysis.

3.4. Selection of colocated 500 m and 30 m pixels with the same land cover

Only one 30 m Landsat 5 and 7 reflectance pair per MODIS 500 m pixel was used to reduce the data volume and to provide a convenient way to investigate the use of MODIS BRDF spectral model parameters for different land cover types. The MODIS land cover product (MCD12Q1) was used to select 500 m pixel locations across the CONUS that were classified consistently as the same land cover class and with classification confidence >50% over eleven years (2002 to 2012). This increased the likelihood that only reliably classified pixels were considered and that the land cover was unchanged at 500 m resolution in 2010 (the year with the winter and summer weeks of Landsat data). Often this filtering eroded the edges of regions that had the same land cover. Fig. 3 illustrates the impact of this filtering for a single 2010 MCD12Q1 tile (left) and the reduced number of 500 m pixels with consistently high confidence land cover types (middle).

For each selected MODIS 500 m pixel a single 30 m pixel location with the same land cover type was selected. This was not straightforward because the spatial arrangement of land cover may be different at 500 m and 30 m and the only available CONUS 30 m land cover

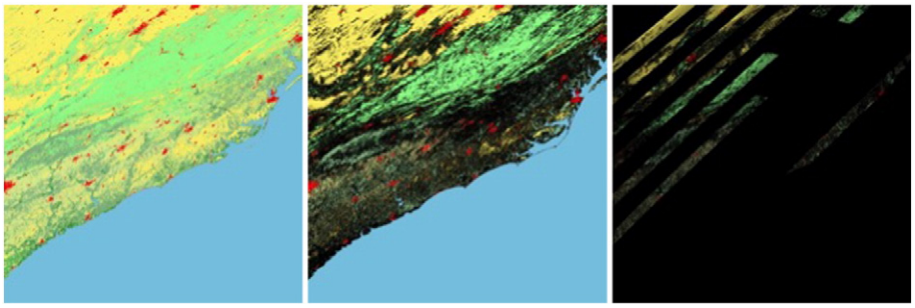

Fig. 3. Illustration of selection of colocated 500 m and 30 m pixels with the same land cover. Left: example MCD12Q1 500 m land cover product (colors correspond to different land cover classes, Table 1) for 2010 MODIS land tile h11v05 (covering approximately 1200 × 1200 km, 91.3785° to 69.2724°W, 30.0000° to 40.0000°N), Middle: same as left but only showing 500 m pixels that had the same MCD12Q1 land cover class label over eleven years (2002 to 2012) and classification confidence >50%; Right: same as middle but showing the 500 m MODIS pixels with a selected summer Landsat 30 m pixel.

products do not have the same class nomenclature as MCD12Q1 (Hansen et al., 2014; Homer et al., 2015). Consequently, the following selection process was implemented by examination of the pairs of Landsat 5 and 7 data, and was undertaken independently for the winter and summer Landsat data.

First, the spectral centroid of all the 30 m Landsat pixel values falling within the selected 500 m MODIS pixel was defined as:

$$\boldsymbol{\rho}_c = \sum_{i=1}^{n} \boldsymbol{\rho}_i / n$$
$$\boldsymbol{\rho}_i = [\rho_i^{\mathrm{ETM+1}}, \rho_i^{\mathrm{ETM+2}}, \rho_i^{\mathrm{ETM+3}}, \rho_i^{\mathrm{ETM+4}}, \rho_i^{\mathrm{ETM+5}}, \rho_i^{\mathrm{ETM+7}}, \rho_i^{\mathrm{TM1}}, \rho_i^{\mathrm{TM2}}, \rho_i^{\mathrm{TM3}}, \rho_i^{\mathrm{TM4}}, \rho_i^{\mathrm{TM5}}, \rho_i^{\mathrm{TM7}}] \quad (3)$$

where $\boldsymbol{\rho}_c$ is the spectral centroid (a vector of six Landsat 5 TM and six Landsat 7 ETM+ surface reflectance values) of the n pixels with overlapping pairs of Landsat 5 and 7 reflectance values that fall within the 500 m pixel.

Second, the 30 m pixel that was closest to the spectral centroid was selected as the one with the minimal value of:

$$\Delta = \sum_{j=1}^{12} \left| \rho_i^j - \rho_c^j \right| \quad (4)$$

where ρ_c is the spectral centroid vector and ρ_i are the reflectance values as Eq. (3). If several 30 m pixels had the same value of Eq. (4) then one was selected at random. The underlying assumption of Eqs. (3) and (4) is that the majority of the 30 m pixels have the same land cover as the 500 m pixel. Consequently, only MODIS 500 m pixels that were more than 50% covered by valid (cloud-free, snow-free, unsaturated) overlapping pairs of Landsat 5 and 7 reflectance values were considered. Fig. 3 (right) illustrates the 500 m MODIS pixels that had corresponding selected 30 m pixels. The diagonal stripe pattern is due to the geometry of the overlapping Landsat 5 and 7 observations (Fig. 1).

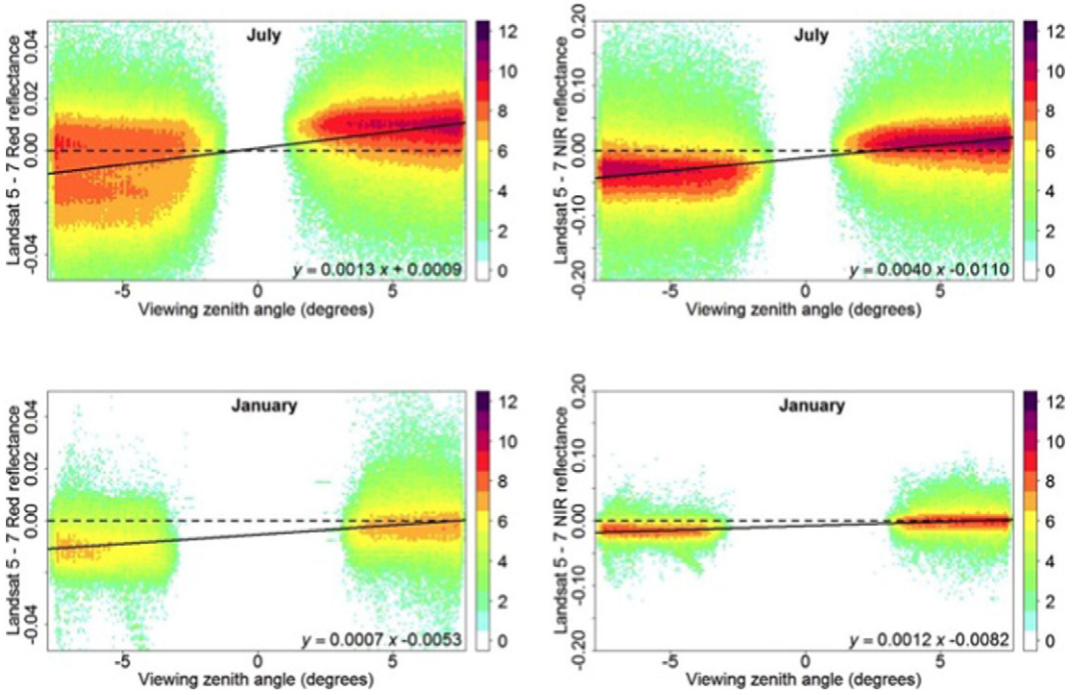

Fig. 4. Scatterplots of observed surface reflectance difference (Landsat 5 TM − Landsat 7 ETM+) versus Landsat 5 TM view zenith angle for the red (left column) and NIR (right column) bands, for the summer (top row) and winter (bottom row) weeks of CONUS data for January and July 2010 (Fig. 1). The colors show the relative frequency of occurrence of similar reflectance difference values (with a $\log_2$ scale); the numbers of overlapping pairs of sensor 30 m reflectance values are summarized in Table 2. The solid lines show ordinary least squares linear regression fits of these data (see Table 3).

Table 2
Total number (n) of pairs of Landsat-5 TM and Landsat-7 ETM+ surface reflectance values for the CONUS July and January data (locations shown in Fig. 1), and the Landsat-5 TM and Landsat-7 ETM+ mean absolute surface reflectance differences ($\overline{\Delta\rho}_\lambda$, Eq. (5)) and relative percentage differences ($\overline{\Delta\rho}^*_\lambda$, Eq. (6)). All data subject to the filtering described in Section 3.

Landsat band	July			January		
	n	$\overline{\Delta\rho}_\lambda$	$\overline{\Delta\rho}^*_\lambda$	n	$\overline{\Delta\rho}_\lambda$	$\overline{\Delta\rho}^*_\lambda$
1 (blue)	1,279,827	0.0098	19.13	185,783	0.0100	14.76
2 (green)	1,375,321	0.0109	14.62	187,409	0.0095	11.22
3 (red)	1,353,843	0.0114	18.13	186,264	0.0091	8.76
4 (NIR)	1,401,725	0.0309	10.73	185,257	0.0129	6.68
5 (1.6 μm)	1,400,499	0.0251	13.08	182,866	0.0136	6.91
7 (2.1 μm)	1,395,513	0.0179	14.96	183,292	0.0121	9.87

3.5. MODIS spectral BRDF model parameter pre-processing to select only high-quality parameters

Only the highest quality snow-free MODIS spectral BRDF model parameters were used. The MODIS spectral BRDF model parameter quality depends on a number of factors including the number and the angular sampling of the reflectance values used in the MODIS BRDF model inversion and the constancy of the surface conditions (Lucht & Lewis, 2000; Schaaf et al., 2002, 2011). The 500 m band-specific BRDF model inversion quality is stored in the Collection 5 MODIS BRDF/Albedo quality product (MCD43A2) and coded 0, 1, 2, 3, or 4 indicating decreasing inversion quality. In this study, only the very highest quality BRDF full inversions, i.e., coded as 0 in the MCD43A2 product were used. In addition, only snow-free MODIS BRDF inversions labeled in the MCD43A2 product were used.

4. Analysis methodology

4.1. Quantification of observed Landsat directional reflectance effects

Before any BRDF normalization was undertaken the surface reflectance differences between the pairs of Landsat 5 TM and Landsat 7 ETM+ values were examined to provide insights into the magnitude of Landsat BRDF effects. The mean absolute reflectance difference and also the relative absolute percentage reflectance difference, were derived for each band as:

$$\overline{\Delta\rho}_\lambda = \frac{\sum_{i=1}^{n}\left|\rho_i^{TM,\lambda} - \rho_i^{ETM+,\lambda}\right|}{n} \quad (5)$$

$$\overline{\Delta\rho}^*_\lambda = \left(\frac{\sum_{i=1}^{n} 2\left|\rho_i^{TM,\lambda} - \rho_i^{ETM+,\lambda}\right| \Big/ \left|\rho_i^{TM,\lambda} + \rho_i^{ETM+,\lambda}\right|}{n}\right) 100 \quad (6)$$

where $\overline{\Delta\rho}_\lambda$ and $\overline{\Delta\rho}^*_\lambda$ are the mean absolute and the relative absolute percentage reflectance differences respectively, $\rho_i^{TM,\lambda}$ and $\rho_i^{ETM+,\lambda}$ is a pair of Landsat 5 TM and Landsat 7 ETM+ surface reflectance values, and there are n pairs for spectral band λ. As each pair is sensed with similar solar geometry but different viewing geometry, specifically the reflectance is sensed in the forward scattering direction from one sensor and the backward scattering direction from the other sensor (Fig. 1), these measures provide an indication of view zenith Landsat BRDF effects. We note that there are several other sources of between sensor difference that may vary spectrally and also with the surface reflectance. These include the slightly different spectral response functions between the Landsat 5 TM and Landsat 7 ETM+ sensors (Steven, Malthus, Baret, Xu, & Chopping, 2003; Teillet et al., 2001) and the different sensor radiometric calibration uncertainties (7% for Landsat 5 TM and 5% for Landsat 7 ETM+) (Markham & Helder, 2012). In addition, although surface changes are unlikely to occur within the one day separation between the Landsat 5 TM and Landsat 7 ETM+ observations, and the majority of changes will be removed by the filtering of Eq. (2), the atmosphere may change in one day. This may inflate values of $\overline{\Delta\rho}_\lambda$ and $\overline{\Delta\rho}^*_\lambda$ because the Landsat surface reflectance correction is imperfect; for example, the mean relative residual in Landsat 7 ETM+ LEDAPS atmospherically corrected data was reported as 5.9% and 4.8% in the red and NIR bands respectively (Ju, Roy, Vermote, Masek, & Kovalskyy, 2012).

Spectral scatter plots and ordinary least regression (OLS) fits of the difference between the observed Landsat 5 TM and Landsat 7 ETM+ reflectance pairs as a function of the view zenith angle were generated for the winter and summer Landsat data independently for each band (blue, green, red, near-infrared and the two shortwave infrared bands). The slopes of the OLS regressions were derived to quantify the average spectral BRDF effect across the Landsat 15.0° field of view. The goodness of fit of the OLS regressions were defined by the coefficient of determination (r^2) and the significance of the OLS regressions was defined by examination of the regression overall F-statistic p-value. The average maximum magnitude of Landsat view zenith BRDF effects was derived by multiplying the OLS slope term by 15.0° and is termed for convenience the B–F difference. The B–F difference captures the average difference between Landsat surface reflectance in the forward and backward scatter directions at the Landsat scan edges.

4.2. Landsat 30 m NBAR derivation using different MODIS spectral BRDF model parameters

The c-factor approach (Roy et al., 2008) that can adjust Landsat reflectance to a specified viewing and solar geometry was used to independently normalize the pairs of Landsat 5 TM and Landsat 7 ETM+ reflectance values to nadir BRDF adjusted reflectance (NBAR) equivalents as:

$$\mathrm{NBAR}_\lambda^{sensor}\left(\theta_v = 0, \theta_s = \frac{\theta_s^{TM} + \theta_s^{ETM+}}{2}\right) = c(\lambda) \times \rho_\lambda^{\mathrm{Landsat}}\left(\theta_v^{sensor}, \theta_s^{sensor}\right)$$
$$c(\lambda) = \frac{\hat{\rho}_\lambda^{\mathrm{MODIS}}\left(\theta_v = 0, \theta_s = \frac{\theta_s^{TM} + \theta_s^{ETM+}}{2}\right)}{\rho_\lambda^{\mathrm{MODIS}}\left(\theta_v^{sensor}, \theta_s^{sensor}\right)} \quad (7)$$

Table 3
Summary of the ordinary least squares (OLS) linear regressions illustrated in Fig. 3 and for the other Landsat bands considered in this study. Δ = (Landsat 5 TM − Landsat 7 ETM+ surface reflectance), θ_v = Landsat 5 TM view zenith angle. The OLS regression coefficient of determination (r^2), the OLS regression F-test p-value, and the B–F difference are shown. The number of data points, i.e., number of pairs of sensor 30 m reflectance values for each band, are summarized in Table 2.

Landsat band	July			January		
	OLS equation	OLS r^2 (p-value)	B–F difference	OLS equation	OLS r^2 (p-value)	B–F difference
1 (blue)	$\Delta = -0.0024 + 0.0013\,\theta_v$	0.3380 (<0.0001)	0.0202	$\Delta = -0.0064 + 0.0011\,\theta_v$	0.2824 (<0.0001)	0.0176
2 (green)	$\Delta = 0.0019 + 0.0013\,\theta_v$	0.3033 (<0.0001)	0.0208	$\Delta = -0.0050 + 0.0007\,\theta_v$	0.1223 (<0.0001)	0.0113
3 (red)	$\Delta = 0.0009 + 0.0013\,\theta_v$	0.2221 (<0.0001)	0.0197	$\Delta = -0.0053 + 0.0007\,\theta_v$	0.1112 (<0.0001)	0.0107
4 (NIR)	$\Delta = -0.0110 + 0.0040\,\theta_v$	0.2753 (<0.0001)	0.0623	$\Delta = -0.0082 + 0.0012\,\theta_v$	0.1734 (<0.0001)	0.0188
5 (1.6 μm)	$\Delta = -0.0036 + 0.0033\,\theta_v$	0.2647 (<0.0001)	0.0505	$\Delta = 0.0019 + 0.0012\,\theta_v$	0.1133 (<0.0001)	0.0184
7 (2.1 μm)	$\Delta = 0.0034 + 0.0022\,\theta_v$	0.2203 (<0.0001)	0.0335	$\Delta = 0.0048 + 0.0008\,\theta_v$	0.0742 (<0.0001)	0.0126

where *sensor* is TM or ETM+ to denote the Landsat 5 TM or Landsat 7 ETM+ sensors respectively, and each pair of $NBAR_\lambda^{TM}$ and $NBAR_\lambda^{ETM+}$ values was defined with a solar zenith angle set as the mean of the observed solar zenith angles of the Landsat 5 TM (θ_s^{TM}) and 7 ETM+ (θ_s^{ETM+}) observations (that typically have only a 0.2° solar zenith difference for the Landsat pairs used in this study due to their one day separation) and nadir view zenith angle ($\theta_v = 0°$). Definition of the azimuthal angles is unimportant because at nadir the BRDF is independent of the azimuthal geometry. The NBAR values were derived for the Landsat blue, green, red, near-infrared and two shortwave infrared bands. The spectrally corresponding MODIS BRDF model parameters, $f_{iso}(\lambda_{MODIS})$, $f_{vol}(\lambda_{MODIS})$, and $f_{geo}(\lambda_{MODIS})$, were used to predict MODIS spectral reflectance (ρ^{MODIS}) for the prescribed viewing and solar geometry as Eq. (1). The MODIS spectral BRDF parameters were defined in a number of different ways described below.

4.2.1. Conventional Landsat NBAR derivation

Each pair of Landsat 5 TM and Landsat 7 ETM+ winter and summer reflectance values was normalized to NBAR as Eq. (7) in the conventional manner (Roy et al., 2008) using the local spatially and temporally contemporaneous 500 m MODIS spectral BRDF model parameters. Only the highest quality snow-free Collection 5 MODIS spectral BRDF model parameters defined on the closest day to the Landsat 5 and 7 pixel acquisition days were used. If there were no high quality snow-free MODIS spectral BRDF model parameters within 8 days then the NBAR derivation was not undertaken (note that the Collection 6 MODIS BRDF parameters will be retrieved daily, simplifying this methodology in the future).

4.2.2. Landsat NBAR derivation using fixed MODIS spectral BRDF model parameters

Rather than use the local spatially and temporally contemporaneous MODIS spectral BRDF model parameters (as in Section 4.2.1), fixed spectral BRDF model parameters were defined in four different ways by averaging the 500 m MODIS BRDF spectral parameters over different spatial and temporal periods. Specifically, the mean values of $f_{iso}(\lambda_{MODIS})$, $f_{vol}(\lambda_{MODIS})$, and $f_{geo}(\lambda_{MODIS})$ were calculated considering the highest quality and snow-free value extracted from *all* of the:

(a) global MCD43 500 m product pixels for 12 months of 2010,
(b) CONUS MCD43 500 m product pixels for 12 months of 2010,
(c) CONUS MCD43 500 m product pixels with colocated 30 m pairs of Landsat 5 and 7 summer (July) reflectance values,
(d) CONUS MCD43 500 m product pixels with colocated 30 m pairs of Landsat 5 and 7 winter (January) reflectance values.

To provide insights into the BRDF shapes and magnitudes provided by the above four sets of spectral BRDF model parameters, plots of ρ^{MODIS} ((1)) and $c(\lambda)$ ((7)) as a function of view zenith angle and different solar zenith angles (0°, 30° or 45°) were examined. To save space, the plots were derived for only the red and near-infrared (NIR) bands. The red and NIR bands were selected as they in particular capture vegetation and soil reflectance differences.

4.3. Landsat NBAR evaluation

If the BRDF normalization is reliable then the NBAR values of each pair of Landsat 5 TM and Landsat 7 ETM+ observations should be similar. To examine this, the mean and relative absolute percentage NBAR differences were derived as:

$$\overline{\Delta NBAR}_\lambda = \frac{\sum_{i=1}^{n} \left| NBAR_i^{TM,\lambda} - NBAR_i^{ETM+,\lambda} \right|}{n} \quad (8)$$

Table 4
Fixed MODIS spectral BRDF model parameters (see Section 4.2.2 for details) for the Red and NIR bands derived by averaging the 500 m MODIS BRDF (MCD43) highest quality and snow-free spectral parameters over different spatial and temporal periods.

MODIS spectral BRDF model parameter set	Red band			NIR band		
	f_{iso}	f_{geo}	f_{vol}	f_{iso}	f_{geo}	f_{vol}
(a) Global 12 months	0.1690	0.0227	0.0574	0.3093	0.0330	0.1535
(b) CONUS 12 months	0.1131	0.0247	0.0462	0.2869	0.0367	0.1833
(c) CONUS July	0.1059	0.0233	0.0409	0.3155	0.0420	0.2108
(d) CONUS January	0.1159	0.0229	0.0296	0.2345	0.0373	0.0979

$$\overline{\Delta NBAR}_\lambda^{*} = \left(\frac{\sum_{i=1}^{n} 2^{\left| NBAR_i^{TM,\lambda} - NBAR_i^{ETM+,\lambda} \right| \Big/ \left| NBAR_i^{TM,\lambda} + NBAR_i^{ETM+,\lambda} \right|}}{n} \right) 100 \quad (9)$$

where $\overline{\Delta NBAR}_\lambda$ is the mean absolute NBAR difference derived for spectral band λ from n pairs of Landsat 5 and Landsat 7 NBAR values derived as (7) from the pairs of Landsat 5 TM and Landsat 7 ETM+ reflectance, and $\overline{\Delta NBAR}_\lambda^{*}$ is the mean absolute relative percentage NBAR difference. We do not expect $\overline{\Delta NBAR}_\lambda$ and $\overline{\Delta NBAR}_\lambda^{*}$ to be zero valued because of the sensor calibration, spectral response function, and atmospheric correction differences described earlier (Section 4.1) and because of any errors in the MODIS BRDF retrieval.

4.4. Sensitivity of Landsat NBAR derivation to land cover

Each pair of Landsat 5 TM and Landsat 7 ETM+ surface reflectance values, located at 30 m pixel location i with MODIS land cover class u ($u = 0, 1, \ldots,$ or 16) (Table 1), was normalized to NBAR using the following MODIS spectral BRDF parameters:

i) the conventional, local spatially and temporally contemporaneous, MODIS spectral BRDF parameters (which by definition have the same land cover class as the Landsat 5 and 7 pair); the resulting NBARs are denoted $NBAR_{i,u,u}^{TM,\lambda}$ and $NBAR_{i,u,u}^{ETM+,\lambda}$,
ii) the MODIS spectral BRDF parameters defined by a randomly sampled pixel that had a different land cover class v ($v = 0, 1, \ldots,$ or 16, $v \neq u$); the resulting NBARs are denoted $NBAR_{i,u,v}^{TM,\lambda}$ and $NBAR_{i,u,v}^{ETM+,\lambda}$,
iii) three sets of fixed spectral BRDF model parameters; the resulting NBARs are denoted $NBAR_{i,u,set}^{TM,\lambda}$ and $NBAR_{i,u,set}^{ETM+,\lambda}$ ($set = a, b,$ or c; as defined in Section 4.2.2);

In this way each pair of Landsat 5 TM and Landsat 7 ETM+ surface reflectance values i was normalized to NBAR once as (i), 16 times as (ii), and three times as (iii). Given the very large number of

Table 5
Global 12 month fixed MODIS spectral BRDF model parameters for all the bands. The n values show the number of 500 m highest quality and snow-free MODIS BRDF spectral parameters pixel values considered; n varies spectrally because of the number of high-quality parameters in the MODIS BRDF/Albedo quality product (MCD43A2) varies spectrally.

Landsat band	n	f_{iso}	f_{geo}	f_{vol}
1 (blue)	15,551,077,545	0.0774	0.0079	0.0372
2 (green)	16,362,112,402	0.1306	0.0178	0.0580
3 (red)	16,095,103,393	0.1690	0.0227	0.0574
4 (NIR)	16,260,280,058	0.3093	0.0330	0.1535
5 (1.6 μm)	16,176,131,413	0.3430	0.0453	0.1154
7 (2.1 μm)	16,149,440,059	0.2658	0.0387	0.0639

combinations generated, only 1400 pairs of summer Landsat 5 TM and Landsat 7 ETM + surface reflectance pairs were considered. The 1400 pairs were selected randomly without replacement from the CONUS July filtered data (Section 3).

The mean and relative absolute percentage NBAR differences between the sensors were derived as (8) and (9) but considering each land cover type independently and for (i), (ii) and (iii). This provided quantitative insights into the magnitude of NBAR sensor differences

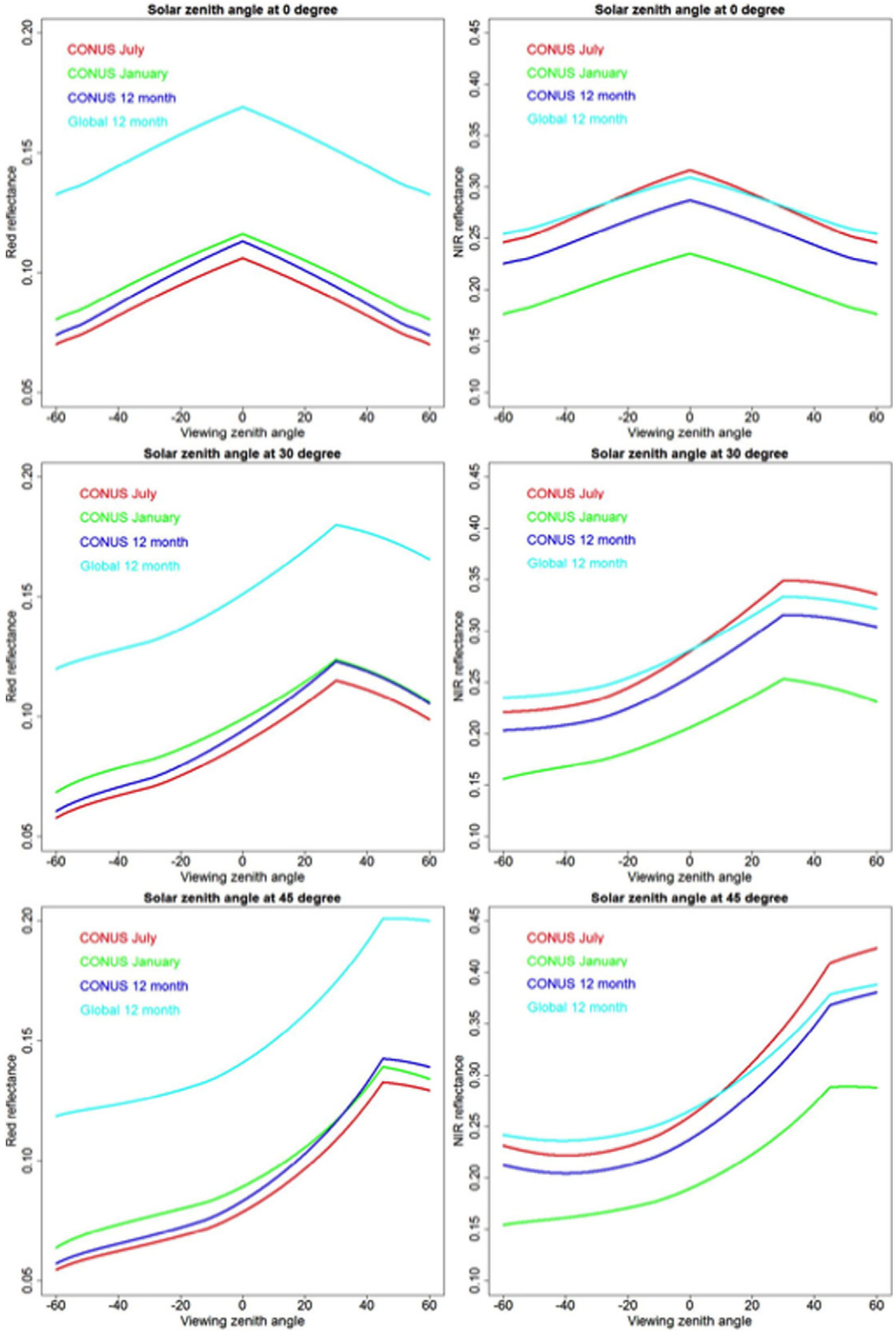

Fig. 5. ρ^{MODIS} derived as (1) for red (left column) and NIR (right column) surface reflectance modeled for MODIS viewing zenith angles (±60°) and for three fixed solar zenith angles (0° top row, 30° middle row, 45° bottom row). The colored lines show the modeled reflectance values for the four sets of fixed MODIS spectral BRDF model parameters (Table 4).

with respect to land cover type and using different spectral BRDF model parameters.

Nominally the local spatially and temporally contemporaneous MODIS spectral BRDF parameters are expected to most appropriate for Landsat NBAR generation. To investigate this, the statistical significance of differences between the NBAR values generated as (i) and as (ii), and between the values generated as (i) and (iii), was quantified. The Landsat 5 and 7 NBAR values derived as (i) ($NBAR^{TM,\lambda}_{i,u,u}$ and $NBAR^{ETM+,\lambda}_{i,u,u}$) was subtracted from the corresponding NBAR values derived as (ii) ($NBAR^{TM,\lambda}_{i,u,v}$ and $NBAR^{ETM+,\lambda}_{i,u,v}$ where $v = 0, 1,$

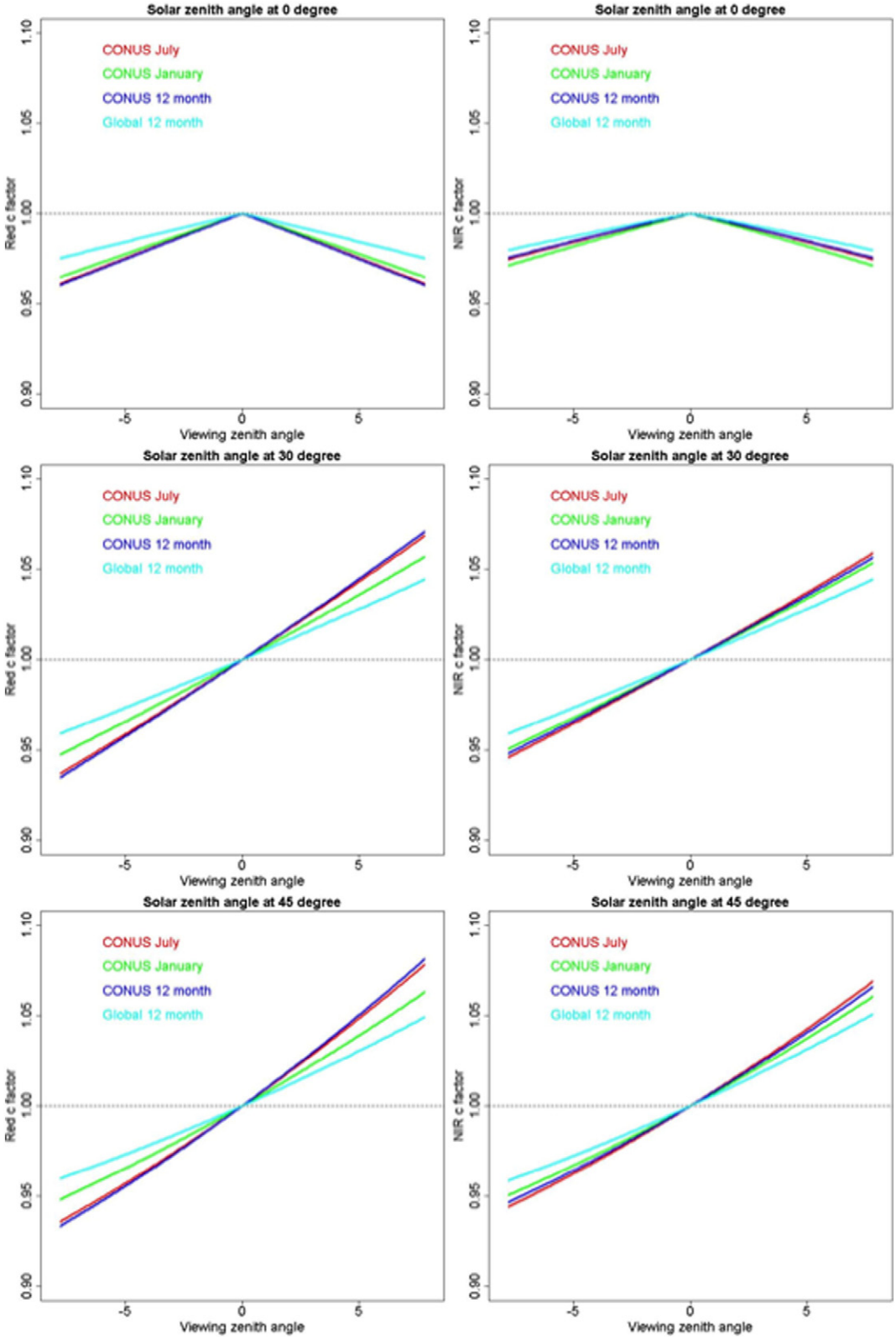

Fig. 6. *c*-factors derived as (7) over the Landsat view zenith angle range ($\pm 7.5°$) for three fixed solar zenith angles (0° top row, 30° middle row, 45° bottom row). The colored lines show the modeled reflectance values for the four sets of fixed MODIS spectral BRDF model parameters (Table 4).

..., or 16, $v \neq u$) to provide a list of NBAR difference values. A two-tailed matched-pairs t-test (Freund & Wilson, 1993) was performed with the null hypothesis that the mean NBAR difference was zero and the alternative hypothesis that the mean difference was not zero. This was undertaken for each spectral band. Similarly, the Landsat 5 and 7 NBAR values derived as (i) ($NBAR^{TM,\lambda}_{i,u,u}$ and $NBAR^{ETM+,\lambda}_{i,u,u}$) were subtracted from the corresponding NBAR values derived as (iii) ($NBAR^{TM,\lambda}_{i,u,set}$ and $NBAR^{ETM+,\lambda}_{i,u,set}$ where $set = a$, b, or c; as defined in Section 4.2.2) and the NBAR difference values were tested for significant differences.

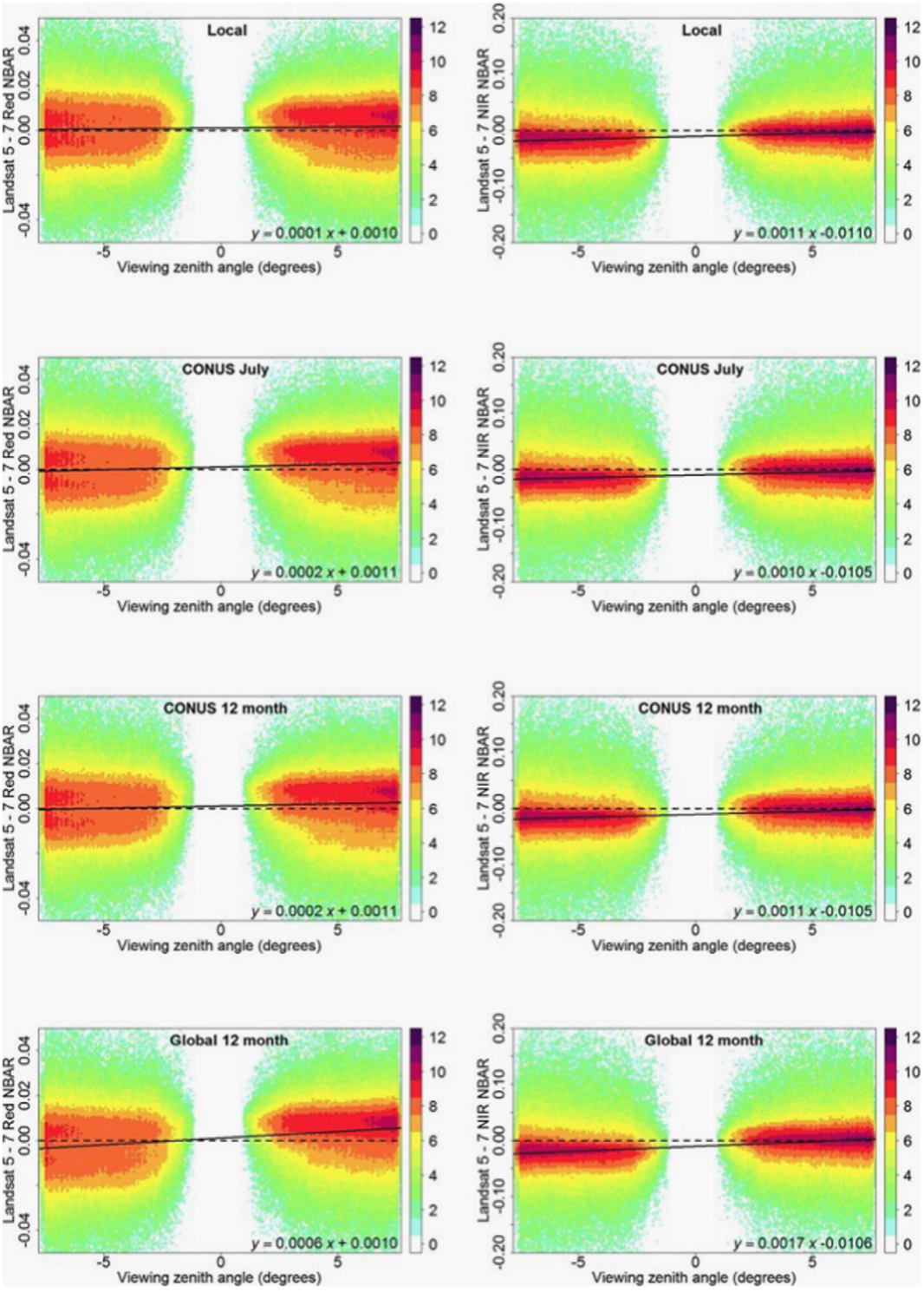

Fig. 7. Scatterplots of NBAR difference (Landsat 5 TM − Landsat 7 ETM+) versus Landsat 5 TM view zenith angle for the red (left column) and NIR (right column) bands. Results for the July data (Fig. 1). The NBAR values derived as (7) using MODIS spectral BRDF model parameters derived using the local spatially and temporally contemporaneous 500 m MODIS spectral BRDF model parameters (top row), and derived using the fixed mean CONUS July (2nd row), CONUS 12 month (3rd row) and Global 12 month (bottom row) model parameters (Table 4). The colors show the relative frequency of occurrence of similar NBAR difference values (with a $\log_2$ scale); the numbers of overlapping pairs of sensor 30 m reflectance values are summarized in Table 2. The solid lines show ordinary least squares regression linear regression fits of these data.

5. Results

5.1. Quantification of observed Landsat bi-directional reflectance effects

Fig. 4 shows scatterplots of Landsat 5 TM and Landsat 7 ETM+ red surface reflectance difference (left column) and NIR surface reflectance difference (right column) as a function of view zenith angle. The plots were generated using all the filtered CONUS data (Section 3) and show more than 1.35 million July (top row) and 185,000 January (bottom row) pairs of Landsat 5 TM and 7 ETM+ surface reflectance values (Table 2). There are fewer Landsat 5 TM and Landsat 7 ETM+ pairs in January than in July because there were fewer winter images available (Fig. 1) and because of greater winter snow and cloud cover. Recall that due to the Landsat sensor overlap acquisition geometry (Fig. 1), each pair of values includes one observed in the forward scattering direction and the other observed in the backward scattering direction. Fig. 4 illustrates an evident view zenith BRDF effect with greater reflectance in the backscatter (shown as positive view zenith angles) than the forward scattering direction. There are no data with absolute view zenith |view zenith| < 0.87° and <1.91° in July and January respectively. This is not because the Landsat 5 and 7 orbits overlap differently in these months but rather because the Landsat orbits overlap more progressively northward (Fig. 1), and further north in the winter the CONUS is predominantly snow covered (Sheng et al., 2015) and generally more cloudy at the time of Landsat overpass (Ju & Roy, 2008).

Table 2 summarizes the mean CONUS absolute ($\overline{\Delta\rho_\lambda}$) and relative percentage ($\overline{\Delta\rho_\lambda^*}$) differences between the pairs of Landsat-5 TM and Landsat-7 ETM+ surface reflectance values. For each band the mean ($\overline{\Delta\rho_\lambda}$) differences are all approximately 0.01 in January data and are greater in July. The mean differences are smallest for the visible bands, greatest for the NIR and intermediate for the shortwave infrared (SWIR) bands. Unsurprisingly, the $\overline{\Delta\rho_\lambda}$ values are greater in July than January suggesting that on average CONUS vegetated surfaces are more anisotropic than winter senescent vegetation and soil dominated surface conditions. The mean relative differences ($\overline{\Delta\rho_\lambda^*}$) are easier to compare between the spectral bands as they are normalized for spectral reflectance differences, whereby, for example, healthy vegetation has low red reflectance but high NIR reflectance. The $\overline{\Delta\rho_\lambda^*}$ differences are greatest for the visible bands and smallest for the NIR band and reflect primarily atmospheric correction errors which are greater at shorter Landsat wavelengths (Ju et al., 2012; Maiersperger et al., 2013).

The solid black lines in Fig. 4 show ordinary least squares (OLS) linear regression fits of the displayed data and are summarized for all the bands in Table 3. The regressions have low r^2 values due to the scatter in the data but are statistically significant ($p < 0.0001$) and all have positive slope terms. The B–F difference, i.e., the OLS slope term multiplied by the Landsat 15.0° field of view, quantifies the average difference between Landsat surface reflectance in the forward and backward scatter directions at the Landsat scan edges. As expected, the B–F differences (Table 3) are greater than $\overline{\Delta\rho_\lambda}$ (Table 2) and, as for the $\overline{\Delta\rho_\lambda}$ values, are smaller in January than July. In January the B–F differences are similar spectrally and vary from around 0.011 to 0.019 whereas in July the B–F differences are about 0.02 in the visible bands, and about 0.03, 0.05 and 0.06, in the 2.1 μm, 1.6 μm and NIR bands respectively (Table 3). These Landsat view zenith BRDF effects are not insignificant and are about an order of magnitude greater than the mean absolute residual due to Landsat 7 ETM+ LEDAPS atmospheric correction errors (Ju et al., 2012).

5.2. Preliminary analysis of fixed MODIS spectral BRDF model parameters

The four sets of fixed MODIS spectral BRDF model parameters (Section 4.2.2) were derived considering more than 15,500,000,000 (global 12 months), 1,200,000,000 (CONUS 12 months), 41.7 million (CONUS July), and 12.9 million (CONUS January) highest quality and snow-free MODIS 500 m pixel values. Table 4 shows the resulting spectral parameters for the red and NIR bands. The f_{vol} and f_{geo} terms act to weight volumetric scattering and geometric-optical BRDF kernels respectively ((1)) and have no direct physical meaning, although they can be conceptualized as describing the directional reflectance effects of inter-leaf and inter-crown canopy gaps respectively (Lucht et al., 2000). The f_{iso} parameter provides an additive reflectance term that reflects nadir viewing and solar geometry ((1)), and so f_{iso} (red) and f_{iso} (NIR) can be considered as average BRDF-independent (i.e., isotropic) red and NIR surface reflectance values. As expected, when considering the three CONUS sets of fixed parameters, the greatest f_{iso} (NIR) and smallest f_{iso} (red) values occur for the July data when vegetation is developed and conversely the smallest f_{iso} (NIR) and greatest f_{iso} (red) values occur for the January data when vegetation is mainly senescent.

The global 12 month MODIS spectral BRDF model parameters are provided for all the bands in Table 5. They are more complex to interpret than the CONUS parameters as they include a much greater diversity of BRDFs representing a larger number of land cover types and conditions and both northern and southern hemisphere vegetation phenology and soil moisture variations. However, they are indicative of a generally soil and vegetation dominated spectra with monotonically increasing f_{iso} values from the blue to 1.6 μm wavelengths and then decreased reflectance at 2.1 μm (Table 5). By averaging all the varying BRDF shapes across the globe or the CONUS, we recognize that we are reducing the BRDF to a single shape.

To provide insights into the BRDF shapes and magnitudes provided by the four sets of spectral BRDF model parameters, plots of ρ^{MODIS} ((1)) as a function of MODIS ±60° view zenith angle and for different fixed solar zenith angles (0°, 30° or 45°) were generated for the red and NIR (Fig. 5). With the sun directly overhead (Fig. 5, top row) ρ^{MODIS} is symmetrical around nadir (view zenith = 0°) whereas for the 30° and 45° solar zenith angles the surface reflectance anisotropy is apparent (Fig. 5, middle and bottom rows) with increased reflectance in the backscatter direction and a hot-spot when the view and solar zenith angles coincide. Two salient observations can be made: (i) the magnitudes of ρ^{MODIS} are different between the four spectral BRDF model parameters, but their shapes are similar, and (ii) the ρ^{MODIS} values vary in an approximately linear manner near-nadir over the narrow Landsat ±7.5° view zenith angle range. This is apparent in Fig. 6 which shows the *c*-factor values for the four sets of spectral BRDF model parameters and for the different fixed solar zenith angles (0°, 30° or 45°) derived over the Landsat ±7.5° view zenith angle range. Recall that the *c*-factor is used to adjust directional reflectance to nadir as (7). Over the narrow Landsat field of view the *c*-factor varies linearly and there is only a marginal difference (no more than 3.20% and 1.81% at the scan edge for

Table 6
CONUS July mean absolute NBAR difference ($\overline{\Delta NBAR_\lambda}$, Eq. (8)) and relative absolute percentage NBAR difference ($\overline{\Delta NBAR_\lambda^*}$, Eq. (9)) values between the *n* pairs (Table 2) of Landsat-5 TM and Landsat-7 ETM+ surface reflectance values normalized to NBAR. The $\overline{\Delta NBAR_\lambda^*}$ values are shown in parentheses under the $\overline{\Delta NBAR_\lambda}$ values. The NBAR was derived for each band using local spatially and temporally contemporaneous 500 m MODIS spectral BRDF model parameters (1st results column) and using different fixed MODIS spectral BRDF model parameters (Table 4) (other result columns).

Landsat band	MODIS spectral BRDF model parameter source			
	Local spatially and temporally contemporaneous	Fixed CONUS July mean	Fixed CONUS 12 month mean	Fixed Global 12 month mean
1 (blue)	0.0075 (15.22)	0.0077 (15.68)	0.0078 (15.83)	0.0083 (16.74)
2 (green)	0.0077 (10.76)	0.0080 (11.33)	0.0080 (11.30)	0.0086 (12.06)
3 (red)	0.0089 (15.37)	0.0091 (15.87)	0.0091 (15.83)	0.0096 (16.42)
4 (NIR)	0.0227 (7.77)	0.0231 (8.00)	0.0233 (8.05)	0.0241 (8.38)
5 (1.6 μm)	0.0164 (8.79)	0.0171 (9.32)	0.0174 (9.52)	0.0189 (10.24)
7 (2.1 μm)	0.0125 (10.99)	0.0129 (11.57)	0.0130 (11.64)	0.0141 (12.46)

Table 7
As Table 6 but for the CONUS January data, the $\overline{\Delta NBAR}^{*}_{\lambda}$ values are shown in parentheses under the $\overline{\Delta NBAR}_{\lambda}$ values.

Landsat band	MODIS spectral BRDF model parameter source			
	Local spatially and temporally contemporaneous	Fixed CONUS January mean	Fixed CONUS 12 month mean	Fixed Global 12 month mean
1 (blue)	0.0096 (14.27)	0.0095 (14.08)	0.0095 (14.01)	0.0095 (14.13)
2 (green)	0.0095 (11.32)	0.0093 (11.09)	0.0094 (11.23)	0.0092 (11.05)
3 (red)	0.0092 (8.83)	0.0090 (8.66)	0.0092 (8.84)	0.0090 (8.59)
4 (NIR)	0.0125 (6.57)	0.0123 (6.44)	0.0124 (6.50)	0.0122 (6.38)
5 (1.6 μm)	0.0116 (6.28)	0.0110 (5.96)	0.0113 (6.07)	0.0108 (5.91)
7 (2.1 μm)	0.0112 (9.24)	0.0107 (9.22)	0.0109 (9.30)	0.0106 (9.27)

the red and NIR bands respectively) among the *c*-factor values derived using the four sets of spectral BRDF model parameters.

5.3. Landsat 30 m NBAR derived using both local spatially and temporally contemporaneous and fixed MODIS spectral BRDF model parameters

Fig. 7 shows scatterplots of the July Landsat 5 TM and Landsat 7 ETM + NBAR differences as a function of view zenith. Tables 6 and 7 summarize the CONUS mean absolute NBAR differences ($\overline{\Delta NBAR}_{\lambda}$) and the relative absolute percentage NBAR differences ($\overline{\Delta NBAR}^{*}_{\lambda}$) for the July and January data respectively. The NBAR values were defined in four different ways using: the local spatially and temporally contemporaneous 500 m MODIS spectral BRDF model parameters (Fig. 7 top row), and using the fixed mean CONUS model parameters (one month and 12 months, Fig. 7 middle rows) and the fixed mean Global 12 month model parameters (Fig. 7 bottom row).

The BRDF effects apparent in the July surface reflectance sensor difference scatterplots (Fig. 4 top row) appear greatly reduced in the equivalent NBAR results (Fig. 7 all rows). The OLS regressions illustrated in Fig. 7 all have low r^2 values (<0.1) but are statistically significant ($p < 0.0001$). The magnitude of the B–F NBAR differences were, for all bands and for both the July and January (not plotted) data, smaller than the corresponding B–F differences for the uncorrected surface reflectance data reported in Table 3. Comparison of the NBAR difference statistics reported in Tables 6 and 7 with the uncorrected surface reflectance sensor difference statistics reported in Table 2 reveals that, for all bands and BRDF parameter sources, the July NBAR differences are always less than the corresponding uncorrected surface reflectance differences. This is also the case for the January NIR and SWIR bands, and the January NBAR differences are comparable to the uncorrected surface

Table 8
July red band mean CONUS absolute NBAR difference ($\overline{\Delta NBAR}_{\lambda}$) and relative absolute percentage NBAR difference ($\overline{\Delta NBAR}^{*}_{\lambda}$) values between the Landsat-5 TM and Landsat-7 ETM + surface reflectance values normalized to NBAR for different land cover types. The $\overline{\Delta NBAR}^{*}_{\lambda}$ values are shown in parentheses under the $\overline{\Delta NBAR}_{\lambda}$ values. The Landsat 5 TM and Landsat 7 ETM + NBAR values were derived using different spectral BRDF model parameters (table rows): the local MODIS BRDF parameters, the three fixed spectral BRDF model parameters (Table 4), and using the incorrect MODIS BRDF parameters defined randomly at other 500 m pixel locations that had different land cover types. The values in bold indicate the smallest $\overline{\Delta NBAR}_{\lambda}$ and $\overline{\Delta NBAR}^{*}_{\lambda}$ in each land cover class column. The red asterisks (*) denote matched-pairs t-test p-values > 0.05 i.e., *no* significant difference between the set of Landsat 5 and 7 NBAR values derived using the local MODIS BRDF parameters and the corresponding set of NBAR values derived using the tabulated spectral BRDF model parameter source.

Spectral BRDF model parameter source	**Land cover class**												
	0 Water	1 Evergreen needleleaf forest	4 Deciduous broadleaf forest	5 Mixed forest	6 Closed shrublands	7 Open shrublands	8 Woody savannas	9 Savannas	10 Grasslands	12 Croplands	13 Urban and built-up	14 Cropland /natural veg. mosaic	16 Barren or sparsely vegetated
Local	0.0143* (54.34)	**0.0067*** **(22.53)**	0.0086* (34.82)	0.0081* (30.72)	0.0077* (9.96)	0.0138* (6.85)	0.0062* (12.42)	0.0052* (5.53)	0.0095* (8.34)	0.0091* (14.55)	**0.0072*** **(10.30)**	0.0074* (15.53)	0.0221* (7.08)
Random Class 0		0.0085 (27.80)	0.0102 (38.76)	0.0084 (31.41)	0.0094* (12.05)	0.0142 (7.05)	0.0078* (14.57)	0.0074 (8.07)	0.0135 (11.59)	0.0120 (17.45)	0.0077 (10.83)	0.0078 (16.34)	0.0227 (7.28)
Random Class 1	0.0164 (56.32)		0.0087 (35.06)	0.0081* (30.46)	**0.0052** **(6.63)**	0.0167 (8.21)	0.0063 (12.58)	0.0051 (5.22)	**0.0092*** (8.17)	0.0094 (14.72)	0.0087* (11.39)	0.0079 (16.44)	0.0235 (7.30)
Random Class 4	0.0180 (58.82)	0.0072* (24.32)		0.0081 (30.83)	0.0107 (13.88)	0.0159 (7.78)	0.0064 (12.59)	0.0057 (6.07)	0.0189 (15.25)	0.0091 **(14.28)**	0.0073* (10.34)	0.0075 (15.69)	0.0393 (12.27)
Random Class 5	0.0143 (53.60)	0.0071 (24.10)	0.0086 (34.88)		0.0063 (8.10)	0.0200 (9.80)	**0.0061** **(12.20)**	**0.0037** **(3.87)**	0.0107 (9.32)	**0.0090** (14.58)	0.0073 (10.53)	0.0085 (17.63)	0.0248 (7.65)
Random Class 6	0.0155* (55.07)	0.0072* (24.29)	0.0085 (34.59)	0.0081* (30.58)		0.0177* (8.67)	0.0063* (12.50)	0.0040* (4.27)	**0.0092*** **(8.11)**	0.0093 (14.47)	0.0075* (10.43)	0.0075* (15.73)	0.0290 (8.98)
Random Class 7	0.0144* (53.75)	0.0082 (27.08)	**0.0082** (33.66)	**0.0080*** (30.48)	0.0095 (12.13)		0.0064* (12.62)	0.0052* (5.58)	0.0097 (8.57)	0.0091* (14.59)	0.0073* (10.43)	**0.0072*** **(15.14)**	0.0217 (6.86)
Random Class 8	0.0153* (54.93)	0.0073 (24.67)	0.0085 (34.53)	**0.0080** (30.32)	0.0107 (13.80)	0.0150* (7.51)		0.0045 (4.82)	**0.0092** (8.14)	0.0091 (14.42)	0.0075* (10.69)	**0.0072** (15.17)	0.0218 (6.84)
Random Class 9	0.0146* (53.97)	0.0076* (25.47)	0.0083 (34.08)	0.0081 (30.51)	0.0098 (12.56)	0.0149* (7.38)	0.0067* (12.92)		**0.0092*** (8.16)	0.0091* (14.51)	0.0074* (10.38)	**0.0072*** (15.27)	0.0218* (6.83)
Random Class 10	0.0152* (54.87)	0.0075* (25.28)	0.0085 (34.69)	0.0081 (30.56)	0.0083 (10.70)	0.0153* (7.52)	0.0062* (12.24)	0.0067* (7.13)		**0.0090** (14.30)	0.0074* (10.38)	0.0073* (15.46)	**0.0214*** (6.74)
Random Class 12	0.0147* (54.21)	0.0072* (24.30)	**0.0082** (33.68)	0.0081 (30.83)	0.0110 (14.22)	0.0157 (7.72)	0.0066 (12.83)	0.0098 (10.50)	0.0108 (9.43)		0.0076* (10.98)	0.0078* (16.49)	0.0231 (7.16)
Random Class 13	0.0145* (53.83)	0.0076* (25.58)	0.0083 (33.97)	0.0081* (30.69)	0.0102 (13.05)	0.0134 (6.65)	0.0064* (12.58)	0.0048 (5.11)	0.0097* (8.53)	**0.0090*** (14.42)		0.0073* (15.43)	0.0245 (7.58)
Random Class 14	0.0153* (54.98)	**0.0067** (22.89)	0.0083* (33.99)	**0.0080** **(30.19)**	0.0083 (10.63)	0.0136 (6.86)	0.0074 (13.97)	0.0125* (13.25)	0.0121 (10.39)	0.0101* (15.81)	0.0074 (10.36)		0.0221 (6.97)
Random Class 16	0.0147* (54.09)	0.0087 (28.51)	0.0084 (34.32)	**0.0080*** (30.41)	0.0130 (16.52)	**0.0131*** **(6.60)**	0.0074* (13.95)	0.0102* (10.89)	0.0143* (12.04)	0.0098* (15.46)	0.0079* (11.40)	**0.0072*** (15.22)	
Fixed CONUS July mean	0.0144* (53.71)	0.0080* (26.72)	**0.0082** (33.82)	**0.0080*** (30.42)	0.0113 (14.50)	0.0135* (6.79)	0.0068* (13.10)	0.0069 (7.44)	0.0105* (9.18)	0.0092* (14.63)	0.0073* (10.53)	**0.0072** (15.17)	0.0217* (6.86)
Fixed CONUS 12 month mean	0.0146* (54.06)	0.0078* (26.09)	0.0083 (34.08)	**0.0080*** (30.46)	0.0103 (13.20)	0.0139* (6.95)	0.0065* (12.72)	0.0060 (6.45)	0.0100* (8.77)	0.0091* (14.50)	0.0073* (10.42)	**0.0072*** (15.25)	**0.0214** **(6.71)**
Fixed Global 12 month mean	**0.0140** **(53.26)**	0.0084 (27.69)	**0.0082** **(33.61)**	**0.0080*** (30.48)	0.0126 (16.02)	0.0132* (6.68)	0.0072* (13.72)	0.0081 (8.73)	0.0114* (9.86)	0.0094* (14.94)	0.0075* (10.87)	**0.0072*** (15.20)	0.0220 (6.99)

reflectance differences in the visible wavelength bands. These results confirm previous research that the MODIS BRDF spectral parameters can be used to reduce Landsat BRDF effects (Flood et al., 2013; Gao et al., 2014; Li et al., 2010; Roy et al., 2008).

The $\overline{\Delta NBAR}_\lambda$ and $\overline{\Delta NBAR}^*_\lambda$ values reported in Tables 6 and 7 are not zero-valued because of the sensor calibration, spectral response function, and atmospheric correction differences described earlier (Section 4.1) and because of any errors in the MODIS BRDF retrieval. The smallest July $\overline{\Delta NBAR}_\lambda$ and $\overline{\Delta NBAR}^*_\lambda$ values are found using the local, then the CONUS July, then the CONUS 12 month, and then the Global 12 month, MODIS spectral BRDF model parameters. This is expected as using local spatially and temporally specific MODIS spectral BRDF model parameters should better capture surface reflectance anisotropy than generalized fixed parameters. Of specific interest however is that the $\overline{\Delta NBAR}_\lambda$ and $\overline{\Delta NBAR}^*_\lambda$ values, in any given spectral band, are only marginally different for the NBAR results generated using the different MODIS spectral BRDF model parameter sources. This suggests that a fixed parameter set may be adequate for Landsat NBAR derivation. This is investigated in the next section.

5.4. Sensitivity of Landsat NBAR derivation to land cover

The sensitivity of the Landsat NBAR derivation to the use of MODIS BRDF spectral model parameters defined with respect to different land cover types was quantified. The purpose was not to examine the average BRDF of different land cover classes, which is expected to depend on several factors, not least the land cover class nomenclature used and the surface condition, but rather to assess if different land cover specific MODIS BRDF spectral model parameters would provide significantly different Landsat BRDF normalization capabilities than those provided by the local parameters. Recall that to manage the considerable number of combinations (Section 4.4) only pairs of Landsat 5 TM and Landsat 7 ETM+ values with at least 1400 July reflectance values per land cover class were considered. For the evergreen broadleaf forest, deciduous needle leaf forest, snow and ice, and permanent wetland classes (Table 1) there were fewer than 1400 Landsat reflectance pairs available, due to the strict filtering used to define the colocated MODIS 500 m and Landsat 30 m pixels (Section 3.4) and because of their relatively sparse occurrence relative to the July Landsat data locations (Fig. 1), and these classes were not considered in this land cover sensitivity analysis. We recognize that evergreen broadleaf and deciduous needle leaf forests (such as certain tropical forest and taiga ecosystems) are not represented in this CONUS land cover sensitivity analysis, but feel that the lessons learned from the other forest classes, that also have typically geometric-optical shadowing (dome) BRDF shapes, are sufficiently illustrative.

To summarize the large number of comparisons, two way matrices were generated with rows and columns defined by the spectral BRDF model parameter types and the land cover class respectively. Tables 8 and 9 summarize for the red and NIR bands respectively the mean CONUS absolute NBAR difference ($\overline{\Delta NBAR}_\lambda$) and relative absolute percentage NBAR difference ($\overline{\Delta NBAR}^*_\lambda$). The water class has the greatest $\overline{\Delta NBAR}^*_\lambda$ values (about 50%) and reflect the inability of the MODIS

Table 9
As Table 8 but $\overline{\Delta NBAR}_\lambda$ and $\overline{\Delta NBAR}^*_\lambda$ values (in parentheses) for the NIR band.

Spectral BRDF model parameter source	Land cover class												
	0 Water	1 Evergreen needleleaf forest	4 Deciduous broadleaf forest	5 Mixed forest	6 Closed shrublands	7 Open shrublands	8 Woody savannas	9 Savannas	10 Grasslands	12 Croplands	13 Urban and built-up	14 Cropland /natural veg. mosaic	16 Barren or sparsely vegetated
Local	0.0172* (48.33)	**0.0119*** **(5.65)**	0.0313* (8.58)	0.0292* (9.62)	0.0132* (6.69)	**0.0120*** **(4.14)**	0.0282* (9.67)	0.0096* (4.43)	0.0184* (7.70)	0.0342* (9.67)	**0.0162*** **(5.76)**	0.0286* (8.01)	0.0216* (5.72)
Random Class 0		0.0205 (9.55)	0.0537 (14.27)	0.0367 (11.95)	0.0116 **(5.84)**	0.0144* (4.95)	0.0363 (12.77)	0.0131 (6.03)	0.0238 (10.10)	0.0374* (10.51)	0.0179 (6.39)	0.0343 (9.53)	0.0308 (7.92)
Random Class 1	0.0177 (48.54)		0.0296* (8.16)	0.0304* (9.97)	**0.0115*** (5.88)	0.0130* (4.48)	**0.0259*** **(8.85)**	**0.0069** **(3.15)**	**0.0181*** (7.60)	0.0335* (9.42)	0.0175* (6.22)	0.0295* (8.20)	0.0272 (7.09)
Random Class 4	0.0170 (47.55)	0.0152 (7.30)		0.0293* (9.64)	0.0194 (9.76)	0.0130* (4.58)	0.0291* (10.07)	0.0121* (5.56)	0.0188* (7.88)	0.0335* (9.48)	0.0166* (5.91)	0.0277 (7.75)	0.0228 (5.96)
Random Class 5	0.0172 (47.91)	0.0152* (7.29)	0.0294 (8.16)		0.0170 (8.55)	0.0140* (4.88)	0.0287* (9.89)	0.0123 (5.68)	0.0192* (8.03)	0.0333* (9.45)	0.0164* (5.82)	0.0290* (8.09)	**0.0206** **(5.39)**
Random Class 6	0.0176 (48.44)	0.0149 (7.06)	**0.0293*** **(8.10)**	0.0293* (9.61)		0.0131* (4.59)	0.0260* (8.89)	0.0071 (3.26)	**0.0181*** **(7.57)**	0.0339* (9.53)	0.0171* (6.07)	**0.0275*** **(7.67)**	0.0259 (6.73)
Random Class 7	0.0172 (47.88)	0.0159* (7.58)	0.0334* (9.12)	**0.0281*** **(9.26)**	0.0178 (8.96)		0.0279* (9.61)	0.0090 (4.13)	0.0184* (7.72)	0.0338* (9.55)	0.0166* (5.87)	0.0290* (8.11)	0.0213 (5.57)
Random Class 8	0.0171* (47.68)	0.0156* (7.48)	0.0297* (8.2)	0.0296* (9.74)	0.0180 (9.06)	0.0123* (4.29)		0.0092* (4.23)	0.0184* (7.68)	0.0333* (9.43)	0.0167* (5.92)	0.0284* (7.94)	0.0209* (5.47)
Random Class 9	0.0170* (47.63)	0.0148* (7.09)	0.0303* (8.36)	0.0292* (9.60)	0.0172* (8.65)	0.0127 (4.40)	0.0290* (10.02)		0.0185* (7.77)	0.0335* (9.45)	0.0164* (5.82)	0.0278* (7.76)	0.0210* (5.50)
Random Class 10	0.0171 (47.78)	0.0142* (6.81)	0.0307 (8.46)	0.0299 (9.81)	0.0171* (8.60)	0.0127* (4.45)	0.0304* (10.52)	0.0122 (5.61)		0.0335* (9.47)	0.0163* (5.79)	0.0286* (7.98)	0.0219 (5.72)
Random Class 12	0.0170* (47.41)	0.0167* (8.02)	0.0365* (9.93)	0.0311 (10.20)	0.0233 (11.66)	0.0129* (4.55)	0.0316* (10.96)	0.0152 (7.02)	0.0209* (8.77)		0.0166* (5.92)	0.0307* (8.56)	0.0218 (5.74)
Random Class 13	0.0173 (48.17)	0.0154* (7.39)	0.0300* (8.27)	0.029* (9.54)	0.0187 (9.42)	0.0124* (4.31)	0.0275* (9.45)	0.0108* (5.00)	0.0184* (7.74)	**0.0330*** **(9.35)**		0.0278* (7.78)	0.0207* (5.43)
Random Class 14	0.0170* (**47.15**)	0.0185 (8.86)	0.0304 (8.36)	0.0304* (9.96)	0.0162 (8.17)	0.0129* (4.57)	0.0302* (10.45)	0.0140* (6.48)	0.0197* (8.25)	0.0345* (9.77)	0.0174* (6.15)		0.0210* (5.53)
Random Class 16	**0.0169*** (47.21)	0.0189 (9.00)	0.0338* (9.24)	0.031 (10.18)	0.0240 (12.03)	0.0138* (4.93)	0.0323* (11.22)	0.0183* (8.42)	0.0239* (10.06)	0.0355* (10.03)	0.0188 (6.66)	0.0300* (8.37)	
Fixed CONUS July mean	0.0170* (47.48)	0.0155* (7.41)	0.0308* (8.46)	0.0291* (9.57)	0.0186 (9.37)	0.0125* (4.38)	0.0288* (9.92)	0.0104 (4.82)	0.0188* (7.85)	0.0336* (9.50)	0.0164* (5.82)	0.0282* (7.87)	0.0207* (5.45)
Fixed CONUS 12 month mean	0.0170* (47.44)	0.0158* (7.55)	0.031* (8.53)	0.0292* (9.60)	0.0191 (9.60)	0.0125 (4.39)	0.0291* (10.03)	0.0109* (5.03)	0.0189* (7.92)	0.0337* (9.54)	0.0165* (5.84)	0.0283* (7.91)	0.0208 (5.46)
Fixed Global 12 month mean	**0.0169*** (47.23)	0.0174 (8.32)	0.033* (9.03)	0.0297* (9.78)	0.0217 (10.90)	0.0131* (4.62)	0.0308* (10.69)	0.0130* (6.01)	0.0197* (8.27)	0.0342* (9.69)	0.0171 (6.07)	0.0294* (8.21)	0.0212* (5.59)

BRDF parameters to reliably model water specular reflectance. In the red band (Table 8), the water, evergreen needleleaf forest, deciduous broadleaf forest, and mixed forest classes have $\overline{\Delta NBAR}^{*}_{\lambda}$ values greater than the approximately 15% all-class $\overline{\Delta NBAR}^{*}_{\lambda}$ value (Table 6). In the NIR band (Table 8), the water, deciduous broadleaf forest, mixed forest, woody savanna and cropland classes have $\overline{\Delta NBAR}^{*}_{\lambda}$ values greater than the approximately 8% all-class $\overline{\Delta NBAR}^{*}_{\lambda}$ value (Table 6). The table values in bold denote the smallest $\overline{\Delta NBAR}_{\lambda}$ and $\overline{\Delta NBAR}^{*}_{\lambda}$ for each land cover class (i.e., the smallest values in each table column). Of the 13 land cover classes considered, the local parameters provide NBAR with the smallest differences between Landsat 5 TM and Landsat 7 ETM + for *only* the evergreen needleleaf forest and urban/built-up classes (red band) and *only* for the evergreen needleleaf forest, open shrubland, and urban/built-up classes (NIR band), which is unsurprising as these are the more structurally dominated (geometric-optically governed) land cover types. The red asterisks (*) denote where there was *no* significant difference between the set of Landsat 5 and 7 NBAR values derived using the local MODIS BRDF parameters and derived using the tabulated spectral BRDF model parameter source. Therefore for the majority of the land cover classes there was no significant difference between NBAR values derived using the local MODIS BRDF parameters and using the incorrect MODIS BRDF parameters (ones that were selected randomly at other 500 m pixel locations that had different land cover types). In the NIR band (Table 9) only the deciduous broadleaf forest, closed shrubland, and barren land cover types provided predominantly significant land cover type differences between using the local and other land cover parameters. In the red band (Table 8) only the water, closed shrubland, savanna and barren land cover types provided predominantly significant land cover type differences between using the local and other land cover parameters.

Considering the fixed MODIS BRDF parameters (bottom rows of Tables 8 and 9), for all the land cover classes, except closed shrubland (red) and closed shrubland and savanna (NIR), there was no significant difference between NBAR values derived using the local and the fixed parameters. In fact in several cases in the NIR the smallest $\overline{\Delta NBAR}_{\lambda}$ and $\overline{\Delta NBAR}^{*}_{\lambda}$ values were found using the fixed rather than the local or random land class parameters.

6. Conclusion and discussion

The need for consistent Landsat data records over space and time for both research and applications is well established and a number of studies have suggested the need for and methods to minimize near-nadir Landsat bidirectional reflectance (BRDF) effects to provide more consistent reflectance data (Broich et al., 2011; Flood et al., 2013; Gao et al., 2014; Hansen et al., 2008; Li et al., 2010; Nagol et al., 2015; Roy et al., 2008; Toivonen et al., 2006). In this comprehensive paper the magnitude of the view zenith BRDF effects observed across a range of surface conditions was quantified and then a general method to normalize Landsat reflectance data to nadir BRDF adjusted reflectance (NBAR) was developed.

A total of 567 CONUS Landsat images acquired over a week in January and July 2010 were examined. The average difference between Landsat 5 TM and Landsat 7 ETM + surface reflectance in the forward and backward scatter directions at the Landsat scan edges were found to be greater in July than in January. In January the differences are about 0.01 in all bands and in July the differences were about 0.02 in the visible bands, and 0.03, 0.05 and 0.06, in the 2.1 μm, 1.6 μm and NIR bands respectively. Thus the magnitude of these Landsat view zenith BRDF effects may constitute a significant source of noise for many Landsat applications, although we note that for certain mapping applications, for example, deforestation (Kennedy, Yang, & Cohen, 2010; Kim et al., 2014; Potapov, Turubanova, & Hansen, 2011) or burned area (Bastarrika, Chuvieco, & Martin, 2011; Boschetti et al., 2015) mapping, these effects may be negligible compared to the surface reflectance signal of interest. The proposed general method to normalize Landsat reflectance to NBAR was found to reduce the average difference between Landsat 5 TM and Landsat 7 ETM + surface reflectance in the forward and backward scatter directions. In July the differences were approximately 0.01 in the visible bands, and 0.01, 0.02 and 0.02, in the 2.1 μm, 1.6 μm and NIR bands respectively. These average differences are not zero valued because of differences imposed by sensor calibration, spectral response function, and atmospheric correction differences between the Landsat 5 and 7 sensors, and because of any errors in the MODIS BRDF product retrieval.

The main finding of this study is that appropriate Landsat NBAR can be generated using a *c-factor* BRDF normalization approach without needing to use local spatially and temporally contemporaneous MODIS BRDF spectral model parameters. The *c-factor* BRDF normalization approach is based on the shape and not the magnitude of the BRDF (Roy et al., 2008). Previous researchers have observed that only a limited number of archetypal BRDF shapes capture most of the variability of the directional reflectance observed in snow-free wide field of view satellite data (Bacour & Bréon, 2005; Jiao et al., 2014; Zhang et al. 2015) and there is little variation in these archetypal shapes in the near-nadir region. Landsat data have a narrow 15° field of view and the results of this study indicate that the BRDF shapes of different terrestrial surfaces are sufficiently similar over this narrow field of view that a *c-factor* BRDF normalization approach may be applied using only a single fixed set of MODIS BRDF spectral model parameters. This has several implications. First, Landsat NBAR can be generated with little sensitivity to the land cover type, condition, or surface disturbance. Thus, Landsat data observed at any location or date can be BRDF normalized in the same way, including surfaces that underwent significant change, for example, due to deforestation or due to fire that can change both the BRDF shape and magnitude (Roy, Lewis, & Justice, 2002; Trigg, Roy, & Flasse, 2005). This is important as the surface state and condition may change due to anthropogenic factors (e.g., urbanization, agricultural crop harvesting and rotation) and due to natural factors (e.g., phenology, wind, fire and other natural disturbances) that are often difficult to detect reliably using Landsat time series (Boschetti et al., 2015; Hansen et al., 2014; Huang et al., 2010; Kennedy et al., 2010; Yan & Roy, 2015; Zhu & Woodcock, 2014). Second, Landsat NBAR can be derived in a computationally efficient manner for all the Landsat global long-term record and prior to the year 2000 availability of the MODIS BRDF/Albedo product. Third, the application of a fixed set of MODIS BRDF spectral model parameters means that the NBAR correction can be removed should a user prefer non-view-angle corrected reflectances.

A general and computationally simple method to normalize snow-free Landsat reflectance data to NBAR is suggested. Namely, the *c-factor* BRDF normalization approach (Eq. (7)) applied using fixed BRDF model parameters (f_{iso}, f_{vol} and f_{geo}) defined for each Landsat band for a specified solar zenith. The global 12 month parameters (Table 5) are recommended as they provide NBAR results sufficiently similar to the other fixed parameters but were derived from more than 15,500,000,000 MCD43 500 m product pixels and so are generally applicable. The proposed method is untested for Landsat NBAR derivation with solar zenith angles that are different from the Landsat overpass solar geometry. Consequently, it is not recommended that the method be used to derive Landsat NBAR with solar zenith angles that are very different from those at the time of Landsat overpass. For large area and multi-temporal applications a smooth predictable parameterization of the observed Landsat 5 and 7 solar zenith for any location and date has been developed (Zhang et al. in press). This approach has been implemented to generate global coverage 30 m Landsat 5 and 7 NBAR surface reflectance data sets that are now available at (http://globalweld.cr.usgs.gov/collections/).

We do not advocate that this method be applied to scanning sensors with wide view angle variations or for the determination of surface albedo, both of which require accurate characterization of the surface

anisotropy which is particularly important in areas of structural complexity where geometric-optical shadowing dominate. However, we note that the general method to normalize Landsat reflectance data to NBAR may be adapted to other sensors that have spectral band passes similar to MODIS and narrow fields of view similar to Landsat. For example, future research to investigate the utility of the method for application to the Sentinel-2 Multi Spectral Instrument (MSI) that has MODIS-like spectral bands and a narrow near-nadir 20.6° field of view only slightly greater than that of Landsat (Drusch et al., 2012) is planned.

Acknowledgments

This research was funded by the U.S. Department of Interior, U.S. Geological Survey (USGS) under grant G12PC00069, by the NASA Making Earth System Data Records for Use in Research Environments (MEaSUREs) program under Cooperative Agreement NNX13AJ24A, and by the NASA MODIS BRDF/Albedo/NBAR product generation grant NNX12AL38G. The U.S. Landsat project management and staff at USGS Earth Resources Observation and Science (EROS) Center, Sioux Falls, South Dakota, are thanked for provision of the Landsat data.

References

Aoki, T., Aoki, T., Fukabori, M., Hachikubo, A., Tachibana, Y., & Nishio, F. (2000). Effects of snow physical parameters on spectral albedo and bidirectional reflectance of snow surface. *Journal of Geophysical Research: Atmospheres (1984–2012)*, *105*, 10219–10236.

Arvidson, T., Goward, S., Gasch, J., & Williams, D. (2006). Landsat-7 long-term acquisition plan. *Photogrammetric Engineering & Remote Sensing*, *72*, 1137–1146.

Bacour, C., & Bréon, F. -M. (2005). Variability of biome reflectance directional signatures as seen by POLDER. *Remote Sensing of Environment*, *98*, 80–95.

Bastarrika, A., Chuvieco, E., & Martin, M.P. (2011). Mapping burned areas from Landsat TM/ETM plus data with a two-phase algorithm: Balancing omission and commission errors. *Remote Sensing of Environment*, *115*, 1003–1012.

Bindschadler, R., Vornberger, P., Fleming, A., Fox, A., Mullins, J., Binnie, D., ... Gorodetzky, D. (2008). The Landsat image mosaic of Antarctica. *Remote Sensing of Environment*, *112*, 4214–4226.

Blanco-Muriel, M., Alarcón-Padilla, D.C., López-Moratalla, T., & Lara-Coira, M. (2001). Computing the solar vector. *Solar Energy*, *70*, 431–441.

Boschetti, L., Roy, D.P., Justice, C.O., & Humber, M.L. (2015). MODIS–Landsat fusion for large area 30 m burned area mapping. *Remote Sensing of Environment*, *161*, 27–42.

Broich, M., Hansen, M.C., Potapov, P., Adusei, B., Lindquist, E., & Stehman, S.V. (2011). Time-series analysis of multi-resolution optical imagery for quantifying forest cover loss in Sumatra and Kalimantan, Indonesia. *International Journal of Applied Earth Observation and Geoinformation*, *13*, 277–291.

Brooks, E.B., Thomas, V., Wynne, R.H., & Coulston, J.W. (2012). Fitting the multitemporal curve: A Fourier series approach to the missing data problem in remote sensing analysis. *IEEE Transactions on Geoscience and Remote Sensing*, *50*, 3340–3353.

Claverie, M., Vermote, E., Franch, B., He, T., Hagolle, O., Kadiri, M., & Masek, J. (2015). Evaluation of medium spatial resolution BRDF-adjustment techniques using multi-angular SPOT4 (Take5) acquisitions. *Remote Sensing*, *7*, 12057–12075.

Drusch, M., Del Bello, U., Carlier, S., Colin, O., Fernandez, V., Gascon, F., ... Martimort, P. (2012). Sentinel-2: ESA's optical high-resolution mission for GMES operational services. *Remote Sensing of Environment*, *120*, 25–36.

Flood, N. (2013). Testing the local applicability of MODIS BRDF parameters for correcting Landsat TM imagery. *Remote Sensing Letters*, *4*, 793–802.

Flood, N., Danaher, T., Gill, T., & Gillingham, S. (2013). An operational scheme for deriving standardised surface reflectance from Landsat TM/ETM + and SPOT HRG imagery for Eastern Australia. *Remote Sensing*, *5*, 83–109.

Flowerdew, R.J., & Haigh, J.D. (1995). An approximation to improve accuracy in the derivation of surface reflectances from multi-look satellite radiometers. *Geophysical Research Letters*, *22*, 1693–1696.

Franch, B., Vermote, E.F., Sobrino, J.A., & Fédèle, E. (2013). Analysis of directional effects on atmospheric correction. *Remote Sensing of Environment*, *128*, 276–288.

Freund, R.J., & Wilson, W.J. (1993). *Statistical methods*. Waltham, Massachusetts, US: Academic Press.

Friedl, M.A., Sulla-Menashe, D., Tan, B., Schneider, A., Ramankutty, N., Sibley, A., & Huang, X. (2010). MODIS collection 5 global land cover: Algorithm refinements and characterization of new datasets. *Remote Sensing of Environment*, *114*, 168–182.

Gao, F., He, T., Masek, J.G., Shuai, Y., Schaaf, C.B., & Wang, Z. (2014). Angular effects and correction for medium resolution sensors to support crop monitoring. *IEEE Journal of Selected Topics in Applied Earth Observations and Remote Sensing*, *7*, 4480–4489.

Gao, F., Schaaf, C., Strahler, A., Jin, Y., & Li, X. (2003). Detecting vegetation structure using a kernel-based BRDF model. *Remote Sensing of Environment*, *86*, 198–205.

Griffiths, P., van der Linden, S., Kuemmerle, T., & Hostert, P. (2013). A pixel-based Landsat compositing algorithm for large area land cover mapping. *IEEE Journal of Selected Topics in Applied Earth Observations and Remote Sensing*, *6*, 2088–2101.

Hall, D.K., Riggs, G.A., Salomonson, V.V., DiGirolamo, N.E., & Bayr, K.J. (2002). MODIS snow-cover products. *Remote Sensing of Environment*, *83*, 181–194.

Hansen, M., Egorov, A., Potapov, P., Stehman, S., Tyukavina, A., Turubanova, S., ... Ju, J. (2014). Monitoring conterminous United States (CONUS) land cover change with web-enabled Landsat data (WELD). *Remote Sensing of Environment*, *140*, 466–484.

Hansen, M.C., & Loveland, T.R. (2012). A review of large area monitoring of land cover change using Landsat data. *Remote Sensing of Environment*, *2012*, 66–74.

Hansen, M.C., Roy, D.P., Lindquist, E., Adusei, B., Justice, C.O., & Altstatt, A. (2008). A method for integrating MODIS and Landsat data for systematic monitoring of forest cover and change in the Congo Basin. *Remote Sensing of Environment*, *112*, 2495–2513.

Hautecœur, O., & Leroy, M.M. (1998). Surface bidirectional reflectance distribution function observed at global scale by POLDER/ADEOS. *Geophysical Research Letters*, *25*, 4197–4200.

Homer, C., Dewitz, J., Yang, L., Jin, S., Danielson, P., Xian, G., ... Megown, K. (2015). Completion of the 2011 National Land Cover Database for the conterminous United States—Representing a decade of land cover change information. *Photogrammetric Engineering & Remote Sensing*, *81*, 345–354.

Hu, B., Lucht, W., & Strahler, A.H. (1999). The interrelationship of atmospheric correction of reflectances and surface BRDF retrieval: A sensitivity study. *IEEE Transactions on Geoscience and Remote Sensing*, *37*(2), 724–738.

Huang, C., Goward, S.N., Masek, J.G., Thomas, N., Zhu, Z., & Vogelmann, J.E. (2010). An automated approach for reconstructing recent forest disturbance history using dense Landsat time series stacks. *Remote Sensing of Environment*, *114*, 183–198.

Irish, R.R., Barker, J.L., Goward, S.N., & Arvidson, T. (2006). Characterization of the Landsat-7 ETM + automated cloud-cover assessment (ACCA) algorithm. *Photogrammetric Engineering & Remote Sensing*, *72*, 1179–1188.

Jackson, R., Teillet, P., Slater, P., Fedosejevs, G., Jasinski, M., Aase, J., & Moran, M. (1990). Bidirectional measurements of surface reflectance for view angle corrections of oblique imagery. *Remote Sensing of Environment*, *32*, 189–202.

Jiao, Z., Hill, M.J., Schaaf, C.B., Zhang, H., Wang, Z., & Li, X. (2014). An Anisotropic Flat Index (AFX) to derive BRDF archetypes from MODIS. *Remote Sensing of Environment*, *141*, 168–187.

Ju, J., & Roy, D.P. (2008). The availability of cloud-free Landsat ETM + data over the conterminous United States and globally. *Remote Sensing of Environment*, *112*, 1196–1211.

Ju, J., Roy, D.P., Vermote, E., Masek, J., & Kovalskyy, V. (2012). Continental-scale validation of MODIS-based and LEDAPS Landsat ETM + atmospheric correction methods. *Remote Sensing of Environment*, *122*, 175–184.

Justice, C., Townshend, J., Vermote, E., Masuoka, E., Wolfe, R., Saleous, N., ... Morisette, J. (2002). An overview of MODIS land data processing and product status. *Remote Sensing of Environment*, *83*, 3–15.

Kennedy, R.E., Yang, Z., & Cohen, W.B. (2010). Detecting trends in forest disturbance and recovery using yearly Landsat time series: 1. LandTrendr—Temporal segmentation algorithms. *Remote Sensing of Environment*, *114*, 2897–2910.

Kim, D. -H., Sexton, J.O., Noojipady, P., Huang, C., Anand, A., Channan, S., ... Townshend, J.R. (2014). Global, Landsat-based forest-cover change from 1990 to 2000. *Remote Sensing of Environment*, *155*, 178–193.

Kovalskyy, V., & Roy, D. (2013). The global availability of Landsat 5 TM and Landsat 7 ETM + land surface observations and implications for global 30 m Landsat data product generation. *Remote Sensing of Environment*, *130*, 280–293.

Lee, D.S., Storey, J.C., Choate, M.J., & Hayes, R.W. (2004). Four years of Landsat-7 on-orbit geometric calibration and performance. *IEEE Transactions on Geoscience and Remote Sensing*, *42*, 2786–2795.

Li, F., Jupp, D.L., Reddy, S., Lymburner, L., Mueller, N., Tan, P., & Islam, A. (2010). An evaluation of the use of atmospheric and BRDF correction to standardize Landsat data. *IEEE Journal of Selected Topics in Applied Earth Observations and Remote Sensing*, *3*, 257–270.

Li, X., & Strahler, A.H. (1992). Geometric-optical bidirectional reflectance modeling of the discrete crown vegetation canopy: Effect of crown shape and mutual shadowing. *IEEE Transactions on Geoscience and Remote Sensing*, *30*, 276–292.

Lindquist, E., Hansen, M., Roy, D., & Justice, C. (2008). The suitability of decadal image data sets for mapping tropical forest cover change in the Democratic Republic of Congo: Implications for the global land survey. *International Journal of Remote Sensing*, *29*, 7269–7275.

Loveland, T.R., & Dwyer, J.L. (2012). Landsat: Building a strong future. *Remote Sensing of Environment*, *122*, 22–29.

Lucht, W., & Lewis, P. (2000). Theoretical noise sensitivity of BRDF and albedo retrieval from the EOS-MODIS and MISR sensors with respect to angular sampling. *International Journal of Remote Sensing*, *21*, 81–98.

Lucht, W., Schaaf, C.B., & Strahler, A.H. (2000). An algorithm for the retrieval of albedo from space using semiempirical BRDF models. *IEEE Transactions on Geoscience and Remote Sensing*, *38*, 977–998.

Maiersperger, T., Scaramuzza, P., Leigh, L., Shrestha, S., Gallo, K., Jenkerson, C., & Dwyer, J. (2013). Characterizing LEDAPS surface reflectance products by comparisons with AERONET, field spectrometer, and MODIS data. *Remote Sensing of Environment*, *136*, 1–13.

Maignan, F., Bréon, F. -M., & Lacaze, R. (2004). Bidirectional reflectance of Earth targets: Evaluation of analytical models using a large set of spaceborne measurements with emphasis on the Hot Spot. *Remote Sensing of Environment*, *90*, 210–220.

Markham, B.L., & Helder, D.L. (2012). Forty-year calibrated record of earth-reflected radiance from Landsat: A review. *Remote Sensing of Environment*, *122*, 30–40.

Markham, B.L., Storey, J.C., Williams, D.L., & Irons, J.R. (2004). Landsat sensor performance: History and current status. *IEEE Transactions on Geoscience and Remote Sensing*, *42*, 2691–2694.

Masek, J.G., Vermote, E.F., Saleous, N.E., Wolfe, R., Hall, F.G., Huemmrich, K.F., ... Teng-Kui, L. (2006). A Landsat surface reflectance dataset for North America, 1990–2000. *IEEE Geoscience and Remote Sensing Letters*, *3*, 68–72.

McIver, D.K., & Friedl, M. (2001). Estimating pixel-scale land cover classification confidence using nonparametric machine learning methods. *IEEE Transactions on Geoscience and Remote Sensing*, *39*, 1959–1968.

Nagol, J.R., Sexton, J.O., Kim, D. -H., Anand, A., Morton, D., Vermote, E., & Townshend, J.R. (2015). Bidirectional effects in Landsat reflectance estimates: Is there a problem to solve? *ISPRS Journal of Photogrammetry and Remote Sensing*, *103*, 129–135.

Ouaidrari, H., & Vermote, E.F. (1999). Operational atmospheric correction of Landsat TM data. *Remote Sensing of Environment*, *70*, 4–15.

Potapov, P., Turubanova, S., & Hansen, M.C. (2011). Regional-scale boreal forest cover and change mapping using Landsat data composites for European Russia. *Remote Sensing of Environment*, *115*, 548–561.

Rahman, H., Verstraete, M.M., & Pinty, B. (1993). Coupled surface-atmosphere reflectance (CSAR) model: 1. Model description and inversion on synthetic data. *Journal of Geophysical Research: Atmospheres*, *98*, 20779–20789.

Roberts, G. (2001). A review of the application of BRDF models to infer land cover parameters at regional and global scales. *Progress in Physical Geography*, *25*, 483–511.

Ross, J. (1981). *The radiation regime and architecture of plant stands*. Norwood, MA, USA: Artech House.

Roujean, J. -L., Leroy, M., & Deschamps, P. -Y. (1992). A bidirectional reflectance model of the Earth's surface for the correction of remote sensing data. *Journal of Geophysical Research: Atmospheres*, *97*, 20455–20468.

Roy, D.P., Qin, Y., Kovalskyy, V., Vermote, E., Ju, J., Egorov, A., ... Yan, L. (2014). Conterminous United States demonstration and characterization of MODIS-based Landsat ETM+ atmospheric correction. *Remote Sensing of Environment*, *140*, 433–449.

Roy, D.P., Wulder, M.A., Loveland, T.R., Woodcock, C.E., Allen, R.G., Anderson, M.C., ... Zhu, Z. (2014). Landsat-8: Science and product vision for terrestrial global change research. *Remote Sensing of Environment*, *145*, 154–172.

Roy, D.P., Ju, J., Kline, K., Scaramuzza, P.L., Kovalskyy, V., Hansen, M., ... Zhang, C. (2010). Web-enabled Landsat data (WELD): Landsat ETM+ composited mosaics of the conterminous United States. *Remote Sensing of Environment*, *114*, 35–49.

Roy, D.P., Ju, J., Lewis, P., Schaaf, C., Gao, F., Hansen, M., & Lindquist, E. (2008). Multi-temporal MODIS–Landsat data fusion for relative radiometric normalization, gap filling, and prediction of Landsat data. *Remote Sensing of Environment*, *112*, 3112–3130.

Roy, D.P., Kovalskyy, V., Zhang, H.K., Vermote, E.F., Yan, L., Kumar, S.S., & Egorov, A. (2016). Characterization of Landsat-7 to Landsat-8 reflective wavelength and normalized difference vegetation index continuity. *Remote Sensing of Environment*. http://dx.doi.org/10.1016/j.rse.2015.12.024 (in press).

Roy, D.P., Lewis, P., & Justice, C. (2002). Burned area mapping using multi-temporal moderate spatial resolution data—A bi-directional reflectance model-based expectation approach. *Remote Sensing of Environment*, *83*, 263–286.

Roy, D.P., Lewis, P., Schaaf, C., Devadiga, S., & Boschetti, L. (2006). The global impact of clouds on the production of MODIS bidirectional reflectance model-based composites for terrestrial monitoring. *IEEE Geoscience and Remote Sensing Letters*, *3*, 452–456.

Scaramuzza, P.L., Bouchard, M., & Dwyer, J.L. (2012). Development of the Landsat data continuity mission cloud-cover assessment algorithms. *IEEE Transactions on Geoscience and Remote Sensing*, *50*, 1140–1154.

Schaaf, C.L.B., Liu, J., Gao, F., & Strahler, A.H. (2011). MODIS albedo and reflectance anisotropy products from Aqua and Terra. In B. Ramachandran, C. Justice, & M. Abrams (Eds.), *Land remote sensing and global environmental change: NASA's Earth observing system and the science of ASTER and MODIS. Remote Sensing and Digital Image Processing Series*, *Vol. 11*, . Springer-Verlag (873 pp.).

Schaaf, C.B., Gao, F., Strahler, A.H., Lucht, W., Li, X., Tsang, T., ... Roy, D. (2002). First operational BRDF, albedo nadir reflectance products from MODIS. *Remote Sensing of Environment*, *83*, 135–148.

Sheng, C., Jian, Z., Mullens, E., Yang, H., Behrangi, A., Yudong, T., ... Xinhua, Z. (2015). Mapping the precipitation type distribution over the contiguous United States using NOAA/NSSL National multi-sensor mosaic QPE. *IEEE Transactions on Geoscience and Remote Sensing*, *53*, 4434–4443.

Steven, M.D., Malthus, T.J., Baret, F., Xu, H., & Chopping, M.J. (2003). Intercalibration of vegetation indices from different sensor systems. *Remote Sensing of Environment*, *88*, 412–422.

Storey, J., Choate, M., & Lee, K. (2014). Landsat 8 operational land imager on-orbit geometric calibration and performance. *Remote Sensing*, *6*, 11127–11152.

Teillet, P., Barker, J., Markham, B., Irish, R., Fedosejevs, G., & Storey, J. (2001). Radiometric cross-calibration of the Landsat-7 ETM+ and Landsat-5 TM sensors based on tandem data sets. *Remote Sensing of Environment*, *78*, 39–54.

Toivonen, T., Kalliola, R., Ruokolainen, K., & Malik, R.N. (2006). Across-path DN gradient in Landsat TM imagery of Amazonian forests: A challenge for image interpretation and mosaicking. *Remote Sensing of Environment*, *100*, 550–562.

Trigg, S., Roy, D., & Flasse, S. (2005). An *in situ* study of the effects of surface anisotropy on the remote sensing of burned savannah. *International Journal of Remote Sensing*, *26*, 4869–4876.

Warren, S.G., Brandt, R.E., & Hinton, P. (1998). Effect of surface roughness on bidirectional reflectance of Antarctic snow. *Journal of Geophysical Research*, *103*, 25.

Wolfe, R.E., Roy, D.P., & Vermote, E. (1998). MODIS land data storage, gridding, and compositing methodology: Level 2 grid. *IEEE Transactions on Geoscience and Remote Sensing*, *36*, 1324–1338.

Yan, L., & Roy, D.P. (2014). Automated crop field extraction from multi-temporal Web Enabled Landsat Data. *Remote Sensing of Environment*, *144*, 42–64.

Yan, L., & Roy, D.P. (2015). Improved time series land cover classification by missing-observation-adaptive nonlinear dimensionality reduction. *Remote Sensing of Environment*, *158*, 478–491.

Zhang, H., Jiao, Z., Dong, Y., & Li, X. (2015). Evaluation of BRDF archetypes for representing surface reflectance anisotropy using MODIS BRDF data. *Remote Sensing*, *7*, 7826–7845.

Zhang, H.K., Roy, D.P., & Kovalskyy, V. (2015). Optimal solar geometry definition for global long-term Landsat time-series bidirectional reflectance normalization. *IEEE Transactions on Geoscience and Remote Sensing*. http://dx.doi.org/10.1109/TGRS.2015.2480684 (in press).

Zhu, Z., & Woodcock, C.E. (2012). Object-based cloud and cloud shadow detection in Landsat imagery. *Remote Sensing of Environment*, *118*, 83–94.

Zhu, Z., & Woodcock, C.E. (2014). Continuous change detection and classification of land cover using all available Landsat data. *Remote Sensing of Environment*, *144*, 152–171.

Zhu, Z., Woodcock, C.E., & Olofsson, P. (2012). Continuous monitoring of forest disturbance using all available Landsat imagery. *Remote Sensing of Environment*, *122*, 75–91.